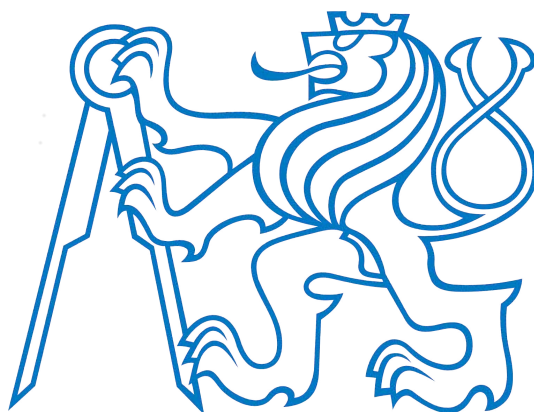


CZECH TECHNICAL UNIVERSITY IN PRAGUE
FACULTY OF ELECTRICAL ENGINEERING



Habilitation Thesis

Flashover performance investigation of polluted and
ice covered insulators exposed to the transient
overvoltages

Radek Prochazka

Prague, September 2015

Contents

1	Introduction	3
2	Transients in Electrical Power System and High Voltage Tests	5
2.1	Short duration power frequency voltage test	6
2.2	Lightning and switching impulse voltage tests	6
2.3	Statistical evaluation of high voltage tests	8
2.3.1	Multiple level test	8
2.3.2	Up and down test method	9
2.3.3	Progressive stress test method	10
2.3.4	Maximum likelihood method	10
2.4	High voltage test procedures	11
2.4.1	Dry test on external insulation	11
2.4.2	Artificial rain tests	12
2.4.3	Freezing condition	13
2.4.4	Ice test procedure	13
2.4.5	Snow test procedures	14
2.4.6	Cold fog procedures	15
3	Measurement of impulse high voltages and currents	16
3.1	Voltage dividers for impulse voltages	16
3.1.1	Determining frequency characteristic of voltage dividers	17
3.1.2	Determining of frequency responses of impulse voltage dividers in frequency domain	19
3.1.3	Using of liquid voltage dividers for fast impulses mea- surement	22
3.2	Rogowski coils for impulse currents measurement	24
3.2.1	Frequency dependency of Rogowski coil constant	26
3.2.2	Influence of Rogowski coil homogeneity to the mea- surement accuracy	33
3.2.3	Influence of Rogowski coil shielding to the measure- ment accuracy	35

3.3	Using of nanocrystalline material for impulse current and voltage measurement	37
3.3.1	Frequency properties of nanocrystalline magnetic cores	38
3.3.2	The application of nanocrystalline magnetic core for impulse current measurement	41
4	The Flashover process in long air gaps	46
4.1	Streamer Breakdown	46
4.2	Streamer propagation	48
4.3	Leader channel formation and advancement	50
5	Experimental flashover performance investigation of polluted and ice covered insulators exposed to impulse voltages	53
5.1	Experimental setup	54
5.2	Ice formation and test procedure	56
5.3	Experimental results	57
5.3.1	Influence of ice thickness on insulator flashover voltage	57
5.3.2	Voltage-time characteristic	59
5.4	Arc propagation along an ice covered insulator	61
6	Mathematical simulation of flashover process	65
6.1	Obenaus basic concept	65
6.1.1	Arc models	66
6.1.2	Resistance of the conductive layer	68
6.2	Dynamic numerical model of discharge propagation on insulator string	71
6.2.1	Simulation process proposal	72
6.2.2	Electric field calculation	73
6.2.3	Simulation results and verification	78
7	Conclusion	81

Chapter 1

Introduction

The high voltage test and measuring technique belong among traditional parts of electric power system. The gradually growing demand for electrical energy causes increasing of transmission voltages. In recent decades, the rapidly increasing of transmission voltages can be observed as a consequence of the development of large hydroelectric power stations far from centers of industrial production. The ultra-high voltage (UHV) transmission systems commonly operate on 1000 kV and the world's highest transmission system in India achieved the value of 1200 kV. At the same time, as the present cost of power electronic elements is reduced, the application of high-voltage direct current transmission (HVDC), flexible ac transmission systems (FACTS) or static synchronous compensator (STATCOM) is increasing. These new trends required extensive development of high voltage engineering, an introduction of many new insulating materials, technologies, test methods and equipments and understanding of discharge processes. All the processes associated with high voltage have essentially stochastic nature. That is what makes this field of study very interesting technical science which is primarily based on laboratory experiments and their verification by calculations. Therefore, apart from the development of high voltage engineering the international standards and equipment for the measurement have to be developed as well. It has been found that some high voltage equipments causes very fast front transients that may damage the insulation system. It opens relevant discussion whether common impulse high voltage tests are sufficient enough or not and if not whether high voltage laboratories can generate and measure such kind of voltages.

Another property of high voltage system which has significant contribution to the mentioned random behavior of high voltage processes, is the fact that majority of insulation systems is exposed to outdoor conditions. The pollution, rain, snow, ice or fog can significantly reduce the electrical strength.

Weather conditions may change rapidly and unpredictably. Moreover, the speed of these changes is still increasing. The sudden appearance of ice and snow is also observed in areas that are not in traditionally cold regions. It was proved that the presence of ice on insulators may lead to insulator flashover and consequent power outages. That is the reason, why many research groups and laboratories are oriented to this wide area. The main objectives of these activities are to extend the knowledge on the influence of atmospheric icing on overhead power transmission lines, on fundamental studies of electrical insulation performance under atmospheric icing and pollution conditions and on flashover mechanisms of ice surfaces. These research activities are very costly whereas the large climatic rooms are needed.

Mentioned facts are motivation for this work which formally can be split into two parts but thematically creates one a whole with a common theme of impulse high voltage testing. The first part is related to the impulse high voltage and current measurement when the main aim of this research is to improve the accuracy of measurement devices for voltage and current impulses and to extend their maximal frequency. It should be noted that there is no comprehensive overview of the whole issue in the text and author presents only results of research works where he was involved. The essential part is focused mainly on research related to Rogowski coil sensor and current and voltage instrument transformers with nanocrystalline magnetic cores and some smaller contribution is related to new constructions of impulse high voltage dividers regarding to their behavior under the very fast impulses.

The second part of this work is related to the flashover performance of suspension insulators exposed to the combination of pollution and icing condition and transient overvoltage. The main objective of this part was experimentally investigate the influence of pollution and ice layer on flashover voltage and on the bases of determined results create a suitable mathematical simulation model. The experimental measurements were performed in Industrial Research Chair on Atmospheric Icing of Power Network Equipment (CIGELE) laboratory which is a research center of University of Quebec in Chicoutimi, Canada. Due to the financial demand of such tests, when the low temperature in climatic room has to be often keep few weeks, the using of mathematical model seemed to be a good idea how to reduce costs in the future. However, the simulation model requires deep knowledge of both physical processes of streamers and leader propagation and calculation of electric field distribution of suspension insulator string. It is almost impossible to take into account all physical aspects of flashover process especially when they are coupled with pollution or ice layer, and some simplification have to be always done. The determined experimental results and the proposal of this model and its validation are objectives of the final chapter of this work.

Chapter 2

Transients in Electrical Power System and High Voltage Tests

Electrical power systems are always subjected to various overvoltages which have the origin in operational manipulations (internal) or atmospheric lightning (external). These overvoltages can reach several times the value of operated voltage with oscillatory or impulse waveforms and different duration. According to IEC standards, we can classify the possible overvoltages as:

- Permanent overvoltages
- Temporary overvoltages
- Transient overvoltages
- Combined overvoltages

Unlike external overvoltages, the internal overvoltages can be very well predicted as they are in a relation to the operated voltage. With increasing of operating voltage the influence of internal overvoltages on insulation design is higher. An insulation system has to be tested to withstand such overvoltages. For these purposes the following main high voltage tests are usually performed:

- Short duration power frequency voltage test
- Switching impulse voltage test
- Lightning impulse voltage test

For today's power systems up to 245 kV the insulation tests are limited to the lightning test and short duration power test and for the voltages above 300 kV the voltage tests include also switching impulse voltage. The requirements and test methods are given by IEC 60060-1 international standard. A brief description of testing methods and evaluation procedures is introduced in the next chapters.

2.1 Short duration power frequency voltage test

The short duration test (60 s) at power frequency is the most common test for insulation systems. For indoor equipment, the test is performed under the dry condition, and the outdoor equipment must be also tested under the prescribed rain condition. The required withstand voltage is derived from the highest voltage for equipment U_m which is the highest rms voltage value in the power system at normal operating conditions. Some typical values are in Table 2.1

U_m (kV)	7.2	12	24	124	245	420
Withstand voltage (kV)	20	28	50	185	325	460

Table 2.1: Standard insulation levels for short term power frequency voltage test according to IEC standards

The high voltage source is usually a testing transformer or cascade of transformers with appropriate power considering wet condition tests when the leakage current is higher than for dry condition. The output voltage has to fulfill the requirements on the sinusoidal waveform that the ratio between the peak value and rms value doesn't exceed the range $\pm 5\%$.

2.2 Lightning and switching impulse voltage tests

As noted, the lightning and switching impulse tests reflect the voltage stress at fast and slow transients in power systems. The standard waveforms were established as a good approximation of the real situation and also can be relatively easy generated in high voltage laboratories. The general lightning and switching impulses are shown in Fig.2.1.

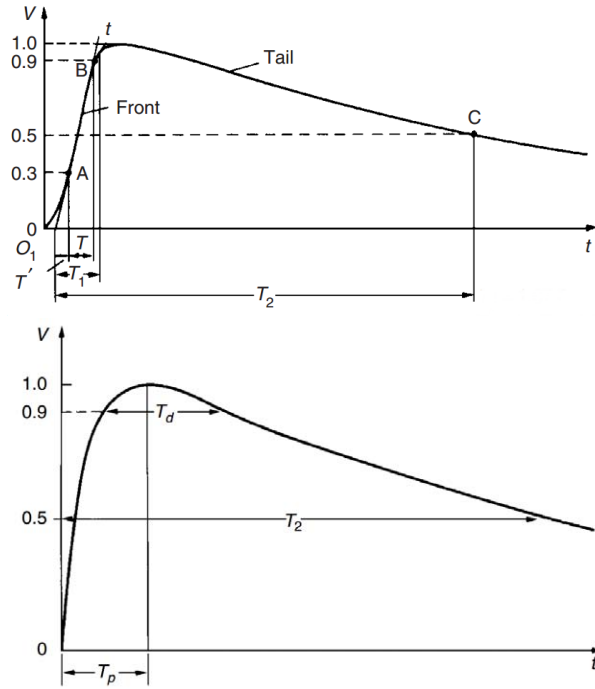


Figure 2.1: General shape of lightning and switching impulse [1]

The impulse parameters with prescribed tolerances are summarized in Table 2.2.

Lightning impulse	$U_p \pm 3 \%$
	$T_1 = 1.2 \mu s \pm 30 \%$
	$T_2 = 50 \mu s \pm 20 \%$
Switching impulse	$U_p \pm 3 \%$
	$T_p = 250 \mu s \pm 20 \%$
	$T_2 = 2500 \mu s \pm 60 \%$

Table 2.2: Lightning and switching impulse parameters and tolerancies

As can be seen in Table 2.2 the allowed tolerances are very wide. This is mainly because each tested object influences the shape of impulses itself (by self capacity and inductance) and it is almost impossible to reach given parameters exactly. Moreover, the capacitance and inductance of the test circuits creates the resonant circuit, and test voltage can be influenced by oscillating component. There is a necessity to evaluate mean curve to eliminate oscillation or overshoot when the frequency of oscillation is not less than 0.5 MHz or the overshoot duration is not greater than 1 μs [2]. With

the development of computer signal processing many algorithms for mean curve determination have been researched, e.g. [3–6]. Some of them are implemented in the automatic evaluation systems for impulse testing in high voltage laboratories. These methods usually work with theoretically derived double exponential model which has a form of subtraction of two exponential functions:

$$u(t) = U_p k (e^{-\tau_1 t} - e^{-\tau_2 t}), \quad (2.1)$$

where U_p is the peak value, k , τ_1 and τ_2 are constants. The constant values for some impulses are shown in Table 2.3.

T_1/T_2	$\alpha_1(s^{-1})$	$\alpha_2 \times 10^3(s^{-1})$	k
1.2/50	14 263	4 876	1.15
1.2/200	3 489	6 245	1.253
250/2500	317	16	1.328

Table 2.3: Table of parameters for various shapes of impulses

The double exponential model is also very often used for the numerical simulations of transients due to lightning or switching voltage impulses in the power system.

2.3 Statistical evaluation of high voltage tests

The electrical discharge phenomena is characterized by a random behavior the statistical methods must be considered. Therefore, the high voltage test should be performed and evaluated on a statistical basis by random experiments and random variables. For high voltage testing the three classes of tests are preferred:

- Multiple level test
- Up-down test
- Progressive stress test

2.3.1 Multiple level test

The multiple level method involves the application of n_i constant voltages at i -th voltage level when $k_i \leq n_i$ trials led to the breakdown. For each voltage level the estimation of breakdown probability is determined, see Fig. 2.2. As

noted Hauschild and Lemke in [7], the relation between the applied voltage and breakdown probability is not a distribution function in the statistical sense but so-called performance function which is not necessarily monotonically increasing. However, in most practical cases the performance function is assumed as monotonically increasing and then can be approximated by theoretical distribution function.

i	n																				k_i	n_i	p_i				
1	-	-	-	-	-	-	-	-	-	-	-	-	-	-	-	-	-	-	-	-	0	25	0				
2	-	-	+	-	-	-	-	-	-	-	-	-	+	-	-	-	-	-	-	+	-	3	25	0.12			
3	-	-	-	-	-	-	+	-	-	-	-	+	-	-	-	-	-	-	-	+	+	+	+	+	7	25	0.28
4	-	+	-	-	-	-	-	-	+	-	-	-	+	-	-	-	-	-	-	-	-	+	-	-	4	25	0.16
5	-	-	-	-	-	-	+	-	-	-	-	+	-	+	+	-	-	-	-	-	+	+	-	-	6	25	0.24
6	-	+	+	+	-	+	-	+	+	+	+	-	+	+	-	+	+	-	+	+	+	-	-	-	12	25	0.48
7	-	-	-	+	+	-	+	-	+	+	+	+	-	-	+	-	-	+	+	+	+	+	+	+	14	25	0.56
8	+	-	+	+	+	+	+	+	+	+	-	+	+	+	+	+	+	+	+	+	+	-	+	+	20	25	0.80
9	+	-	+	-	+	+	+	+	+	+	+	+	+	+	-	+	+	+	+	+	-	-	+	+	19	25	0.76
10	+	+	+	+	+	-	+	+	+	+	+	+	+	+	-	+	+	+	+	+	+	+	+	+	22	25	0.88

Figure 2.2: Example of multilevel method $n_i=25$, $i = 1, 2, \dots, 10$.

In the past, the results were plotted in a spatial probability paper grid to transform the nonlinear probability function to the linear function. Then the approximation can be performed in an easy manner. Nowadays, many mathematical tools for nonlinear regression are available and can be simply implemented into the test evaluation systems. The Normal (Gauss), Weibull or Gumbel probability functions are often used as good approximations in this case.

2.3.2 Up and down test method

In high voltage practice usually it is not necessary to know a whole performance function. The searched values could be the 10 % quantile u_{10} as the voltage with very low probability of breakdown or u_{50} as a mean value estimation. First the voltage step Δu and initial voltage u_0 are selected. Then the voltage is increased or decreased from initial value depending on the previous test result. If the breakdown occurs the voltage is decreased, otherwise the voltage is increased. This procedure is repeated until the predetermined number of trials n is reached. The example of up and down method record for u_{50} is in Fig. 2.3.

The required number of impulses on each voltage level for various orders of quantile p are presented in Tab. 2.4.

The estimation of U_p is given by approximation formula:

the assumption is made that the set of observations x_1, x_2, \dots, x_n is a set of n independent random variables with probability density function $f(x_i, \theta)$ where θ is set of parameters. The maximum likelihood estimate of θ is that value of θ which maximizes the likelihood function L :

$$L(\theta) = \prod_{i=1}^n f(x_i, \theta). \quad (2.4)$$

Rather than maximising this product is often use the logarithm:

$$L(\theta) = \sum_{i=1}^n \ln f(x_i, \theta). \quad (2.5)$$

If it is expected that the observed values x_1, x_2, \dots, x_n are normally distributed $N(\mu, \sigma)$ their probability density function is:

$$f(x_1, x_2, \dots, x_n, \mu, \sigma) = \prod_{i=1}^n \frac{1}{\sigma\sqrt{2\pi}} e^{-\frac{(x_i - \mu)^2}{2\sigma^2}}. \quad (2.6)$$

As the $L(\mu, \sigma)$ function:

$$L(\mu, \sigma) = -\frac{n}{2} \ln 2\pi - n \ln \sigma - \frac{1}{2\sigma^2} \sum_{i=1}^n (x_i - \mu)^2. \quad (2.7)$$

The parameters μ and σ can be determined by solving the equations:

$$\frac{\partial L(\mu, \sigma)}{\partial \mu} = -\frac{n}{\sigma} + \frac{1}{\sigma^3} \sum_{i=1}^n (x_i - \mu)^2 = 0, \quad (2.8)$$

$$\frac{\partial L(\mu, \sigma)}{\partial \sigma} = \frac{1}{\sigma^2} \sum_{i=1}^n (x_i - \mu) = 0. \quad (2.9)$$

2.4 High voltage test procedures

2.4.1 Dry test on external insulation

High voltage tests have to be performed on all external insulation. The breakdown voltage can be affected by the arrangement of a test object. Important are mainly distances to grounded parts, walls or ceiling of the test room and arrangement of high voltage conductors. The clearance to all external structures should be higher than 1.5 times the length of shortest discharge path

along the test object. The atmospheric conditions shall be measured, and the atmospheric correction factor calculated as

$$K_t = k_1 k_2, \quad (2.10)$$

where $k_1 = \delta^m$ and $k_2 = k^w$. The air density δ is determined by temperature t and pressure p :

$$\delta = \frac{p}{p_0} \frac{273 + t_0}{273 + t}, \quad (2.11)$$

where p_0 and t_0 are atmospheric normal conditions ($t_0 = 20 \text{ }^\circ\text{C}$, $p_0 = 101,3 \text{ kPa}$). The correction factor k_2 respects the influence of humidity to breakdown voltage especially when it is determined by partial discharges. Partial discharges depend on the kind of test voltage, and different correction have to be applied. For lightning and switching impulses, the parameter k has a form of:

$$k = 1 + 0.010 \left(\frac{h}{\delta} - 11 \right), \quad (2.12)$$

where h is absolute humidity. Exponents m and w describe the characteristic of possible partial discharges and their values are recommended in [2]. Test engineers very often assume m and w equal to one. The atmospheric correction factor can be used to correct a measured breakdown voltage V to the value under standard atmospheric conditions

$$V_0 = \frac{V}{K_t} \quad (2.13)$$

or to actual test voltage value calculation when the test voltage V_0 is specified for standard atmospheric conditions

$$V = V_0 K_t. \quad (2.14)$$

The procedures for atmospheric corrections are still not perfect, and especially the humidity correction is limited to air gaps. Due to the different absorption of water by different surface materials the humidity correction is not applicable to flashovers along insulating surfaces in the air [7].

2.4.2 Artificial rain tests

The artificial rain test imitates the influence of natural rain to insulation performance of outdoor insulators and is recommended for all types of test

Rain parameters	Unit	Range
- vertical component	<i>mm/min</i>	1 – 2 ± 0.5
- horizontal component	<i>mm/min</i>	1 – 2 ± 0.5
Water temperature	°C	ambient temperature ±15
Water conductivity	<i>μS/cm</i>	100 ± 15

Table 2.5: Water parameters (mean value of all measurements) for artificial rain test according to IEC standard [2]

voltages. The standardized parameters of water used for artificial rain test are summarized in Table 2.5.

Generally, the reproducibility of artificial rain test is lower, and some additional requirements have to be taken into consideration to decrease the variance of results. These requirements are described in detail in [2]. The water should be sprayed uniformly along the test object, and the water conductivity and temperature must be measured on water sample. The conductivity and temperature measurements should be performed before the water impacts on the test object or directly in the storage tank. The test object must be subjected to the artificial rain at least 15 minutes before the voltage test, and consequently the rain is not interrupted when the voltage is applied. The artificial rain test procedure is the same as the adequate procedure at the dry condition. In general, one flashover is allowed at ac and dc withstand voltage test provided that there is no other flashover during repeated test.

2.4.3 Freezing condition

Test procedures, test equipment, and evaluation methods were recommended in IEEE Standard 1783 [8] for the cases when an external insulation is subjected to the combination of contamination, ice, snow and cold fog.

2.4.4 Ice test procedure

Natural conditions are simulated by depositing artificial ice on energized insulators (usually at normal service voltage) in a climate room. The experimental conditions which should be adjusted to form glaze ice (clear ice) with icicles are summarized in Table 2.6

The ice thickness should be measured in the applied water exposure zone on two 25 mm to 30 mm cylinders when one is rotating and second is fixed.

Ice deposit parameter	Recommended value
Type	Glaze ice (clear ice) with icicles
Thickness	5 mm to 30 mm on rotating cylinder
Freezing water flux	60 L/h/m ² ± 20 L/h/m ²
Water conductivity σ_{20}	100 $\mu S/cm$ at 20°C
Air temperature	5 °C to 15 °C
Wind speed	3 m/s to 5 m/s
Precipitation direction	45° ± 10°
Applied voltage	Service voltage stress

Table 2.6: Summary of the recommended ice deposit parameters [8]

The length of both cylinders is about 600 mm. The cylinders should be in the place to receive the same wetting as the insulator under test. The applied water droplet size and wind speed shall be adjusted to give a water droplet direction of about 45° ± 10° from top to bottom, compared to a vertical axis. A preparation period is needed between the end of the ice accretion at a sub-zero temperature and the moment when test voltage is applied for flashover voltage evaluation.

Two procedures should be used: icing regime or melting regime. The icing regime method is faster than melting regime method, but the melting regime methods is more representative of natural conditions. At one laboratory, the two test methods give similar results.

In the icing regime, the flashover performance tests should be carried out shortly after ice accretion is finished, and the water film is still present on the ice surface. Thus, the preparation time is very short (from 2 min to 3 min). At this point, the flashover test is performed.

For the melting regime, the normal system voltage shall be turned off for a minimum of 15 min, after the ice accretion. In this hardening phase, the wind speed shall continue, and the air temperature shall be kept at the icing temperature to ensure complete hardening of the ice and balance of insulator and ice temperatures. Immediately after the hardening sequence the melting sequence should start. The temperature is increased rapidly to 2 °C and then increased linearly at a rate of 2 °C/h to 3 °C/h to a final melting temperature.

2.4.5 Snow test procedures

Two methods of snow deposition were proposed [9]. The first method consists of covering the insulator with soft rime, which is produced from very

small super-cooled water droplets, followed by raising the air temperature to increase the water content. No voltage is applied during the soft-rime accretion. This approach is recommended for simulation of snow on vertical insulators.

The second method consists of covering the insulator with natural snow gathered on the ground. The snow from a pile can be directly used to cover the insulator at sub-zero temperature or blocks of naturally accumulated snow is cut and placed and arranged on insulator. Once the test insulator is covered with snow, cold room temperature is increased to around $0\text{ }^{\circ}\text{C}$ and the volume density, conductivity, height, and water content of snow are measured. The recommended snow deposit parameters are summarized in Table 2.7.

Snow deposit parameter	Recommended value
Type	Natural snow
Thickness	30 <i>cm</i> , 50 <i>cm</i> or 70 <i>cm</i>
Density	0.3 <i>g/cm</i> ³
Snow melted-water conductivity σ_{20}	100 $\mu\text{S/cm}$ at 20 $^{\circ}\text{C}$
Air temperature	$-6^{\circ}\text{C} \pm 1^{\circ}\text{C}$
Location of deposit	Vertically above insulator
Precipitation direction	$45^{\circ} \pm 10^{\circ}$
Applied voltage	Service voltage stress

Table 2.7: Summary of the recommended snow deposit parameters [8]

2.4.6 Cold fog procedures

The cold room is cooled to $-4\text{ }^{\circ}\text{C}$, and the cold-fog is produced using water with a conductivity of approximately $300\ \mu\text{S/cm} \pm 100\ \mu\text{S/cm}$. The median droplet diameter is $10\ \mu\text{m} \pm 3\ \mu\text{m}$. The dew point of the cold room should be monitored. The insulator is energized at service voltage during cold-fog accretion. When the dew point is within $2\text{ }^{\circ}\text{C}$ of ambient temperature and a dense fog is visible, the cold-room temperature is increased from $-4\text{ }^{\circ}\text{C}$ to $-2\text{ }^{\circ}\text{C}$ in no less than 1 h. Air flow should be maintained at about 10 km/h with less than 10 % turbulence intensity. The temperature rise of the test chamber should be $0.6\text{ }^{\circ}\text{C/h}$, from $-2\text{ }^{\circ}\text{C}$ to $1\text{ }^{\circ}\text{C}$ in 5 hours. The dew point should remain within $2\text{ }^{\circ}\text{C}$ of ambient temperature and test voltage should be kept constant, as in the accretion period.

Chapter 3

Measurement of impulse high voltages and currents

Impulse voltage and currents are often used in high voltage laboratories to perform lightning and switching impulse tests. The current waveform can be also used for the test evaluation. The impulse voltages and currents are characterized by fast front time and high amplitudes as was described in Chapter 2. Nowadays, with the increasing number of application based on power semiconductors, some standards starts to require even faster impulse front time then was obvious in the past. The need to measure rapidly changing impulse voltages arises not only in the high voltage testing but also in many research problems in physic. At the same time, there is pressure to improve the overall measurement uncertainty. These factors evoked an activity of international professional working groups and research teams to develop new measurement devices and procedures which fulfill the requirements.

3.1 Voltage dividers for impulse voltages

The voltage dividers are classic measuring devices for dc, ac and impulse voltages up to highest levels of magnitudes (few megavolts). Usually, the complete waveform of impulse voltage is of interest. The actual waveform must not be distorted or overshoot from the measuring system. The three basic types of voltage dividers exist: resistive, capacitive and inductive. From them, the combined voltage divider can be completed. The principle of voltage dividers is very simple and, in general, can be described by formula:

$$\frac{U_2}{U_1} = \frac{Z_2}{Z_1 + Z_2}, \quad (3.1)$$

where Z_1 is high voltage impedance, Z_2 is low voltage impedance, U_2 is output voltage and U_1 is measured voltage. The expression of Z_1 and Z_2 depends on the type of voltage divider. The properties of voltage dividers are described in many books and research papers deal with the high voltage technique, i.e. [1,7,10]. As was mentioned in the previous text, currently the main issues are related to meet the increasing requirements on measurement accuracy and to record correctly impulses with very steep front. These hard requirements can be fulfilled with the voltage dividers with the flat transfer function up the frequencies above 1 MHz. The shape of the transfer function is given by construction of voltage dividers and frequency dependance of used elements.

3.1.1 Determining frequency characteristic of voltage dividers

Investigating the frequency characteristic properties of voltage dividers by frequency response methods brings good insight into the behavior of the measuring device. Usually, from the practical purposes, the step response method is preferred. The input voltage is generated by switching dc voltage of magnitude V_0 . The switch can be realized as a mercury-wetted relay or as a breakdown in pressurized gas or oil, see i.e. [10,11]. Some laboratories use for the evaluation of the step response standard chopped atmospheric impulses [12,13]. The typical normalized step response is shown in Fig. 3.1. Because the large dimensions of high voltage dividers, the lead inductances and stray capacitances are present and causes the superposition of oscillations on the exponentially rising response.

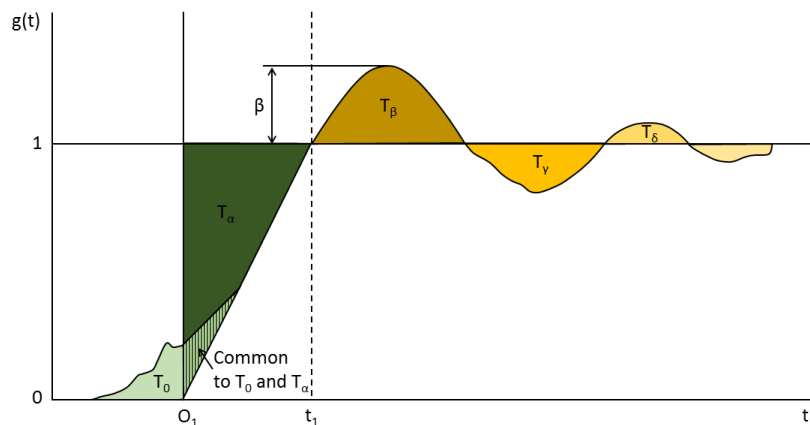


Figure 3.1: Typical normalized step-response of a voltage divider

The response time is defined to represent the area enclosed by the normalized step response, the final value 1 and the axis $t = 0$:

$$T_{res} = \int_{O_1}^{\infty} (1 - g(t)) dt = T_{\alpha} - T_{\beta} + T_{\gamma} - \dots, \quad (3.2)$$

where $g(t)$ is the step response, T_{α} , T_{β} and T_{γ} are the shaded areas in Fig. 3.1. The settling time T_s is then defined as the time from which up to infinity the measured normalized step response will not deviate from the unit level no more than 2% of the settling time. The definition can be mathematically described as

$$T_s = \int_{T_s}^{\infty} |(1 - g(t)) dt| < 0.02T_s. \quad (3.3)$$

Under the assumption that the whole measurement system is linear, causal, and time-shift invariant the output $v_o(t)$ of a system to an arbitrary input $v_i(t)$ is in the time domain given by its convolution with the system impulse response $h(t)$

$$v_o(t) = v_i(t) * h(t). \quad (3.4)$$

Usually the step response is measured, instead of the impulse response $h(t)$, because of the difficulties in producing suitable delta function impulse excitation. The impulse response $h(t)$ can be derived from the normalized unit step response $g(t)$ by calculating the derivative of $g(t)$

$$h(t) = \frac{d}{dt}g(t). \quad (3.5)$$

Because the differentiation operator in convolution is interchangeable, the convolution equation 3.4 can be rewritten as

$$v_o(t) = \frac{d}{dt}v_i(t) * g(t). \quad (3.6)$$

For a numerical calculation the convolution equation can be expressed as the convolution discrete sum

$$v_o(i) = \sum_{k=0}^n v'(k)g(i - k)\Delta t. \quad (3.7)$$

Instead of using convolution calculation the Fourier and inverse Fourier transformation can be another alternative for computation of an output impulse signal [12]. Then, the convolution operator became a pure division and the transfer function $G(j\omega)$ is defined as:

$$G(j\omega) = \frac{V_o(j\omega)}{V_i(j\omega)}, \quad (3.8)$$

where V_o and V_i are Fourier transformations of output and input voltage signals.

For a known step response of a measuring system, considering equation 3.5, the output impulse voltage can be expressed as:

$$v_o(t) = \mathcal{F}^{-1} \left\{ \mathcal{F}\{v_i(t)\} \mathcal{F}\left\{\frac{d}{dt}g(t)\right\} \right\}, \quad (3.9)$$

where \mathcal{F} and \mathcal{F}^{-1} are the symbols for the Fourier and inverse Fourier transformations.

The experimentally measured step response are used for determination of the suitability of a particular measuring system for making measurements of interest. The above described methods for v_o calculations involves the experimental step response with an analytic waveform which represents the ideal waveform expected in the experimental arrangement (i.e. a lightning waveform described by double exponential model with appropriate time constants). If the differences between the input and output voltage peak or time parameters exceed the uncertainty requirements given by standards, the system is inadequate for the measurement of the input waveform used in the calculations.

3.1.2 Determining of frequency responses of impulse voltage dividers in frequency domain

Another way how to determine the frequency response of impulse voltage dividers is a direct measurement in the frequency domain. This method is more demanding then the measurement of step response due to higher requirements on instrumentation and needed time, but gives more precise results. The measurement circuit is shown in Fig. 3.2.

The harmonic voltage, with variable frequency, is generated by the arbitrary generator and amplified to reach well measurable voltage value on the output of voltage divider within the whole range of frequencies. The voltages values and phase is read from the digital scope. Examples of determined frequency dependency of ratio for two common voltage dividers 1 MV and 200 kV is shown in Fig. 3.3. The phase shift dependency between input and output voltages is shown in Fig. 3.4.

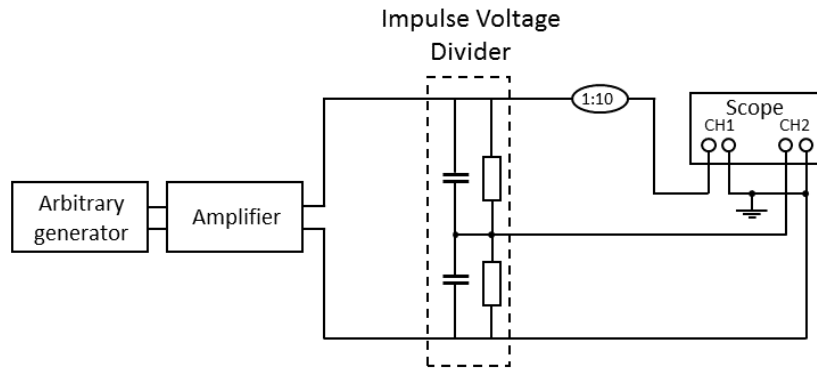


Figure 3.2: Frequency response analysis of impulse voltage divider

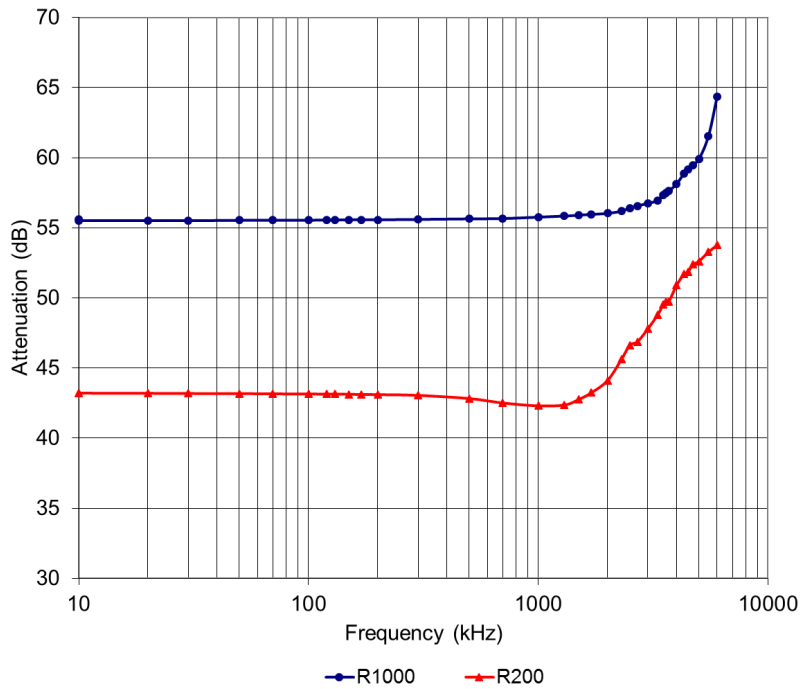


Figure 3.3: Determined attenuation of two common impulse voltage dividers (Haefely R1000 and R200)

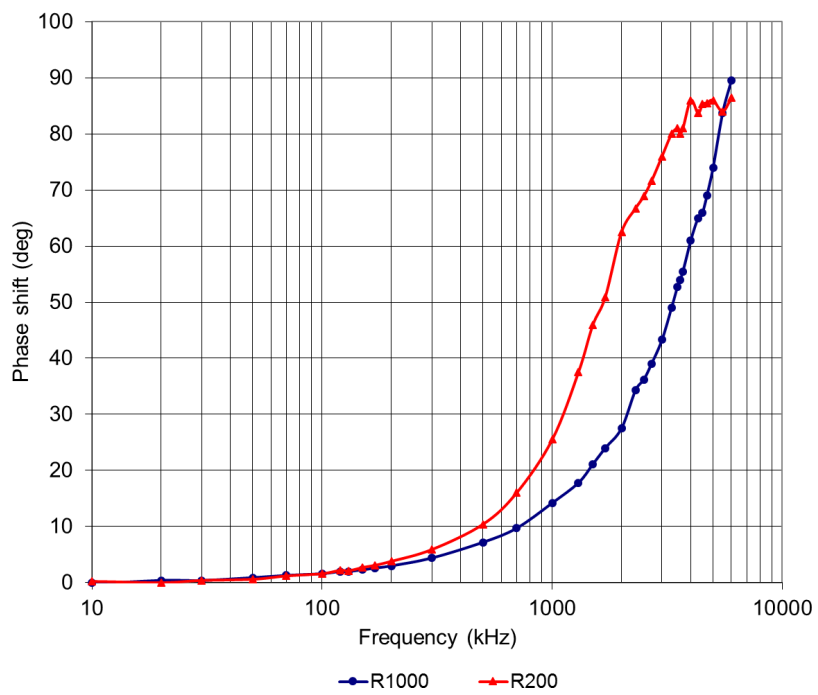


Figure 3.4: Determined phase shift between input and output voltages of two common impulse voltage dividers (Haefely R1000 and R200)

As can be seen from determined frequency characteristics common impulse voltage dividers have relatively constant ratio up to the frequency of 500 kHz. This maximal frequency is sufficient for impulses with the front time $1.2 \mu s$. The new constructions and methods have to be used for measurement of faster impulses to suppress parasitic inductance and capacitance. The research activities in this field are nowadays focused mainly on the using of ceramic disc resistors and liquid voltage dividers.

3.1.3 Using of liquid voltage dividers for fast impulses measurement

Some standards, i.e. IEC 61211, requires the application of fast-rise impulses with a reported rise time of 200 ns at voltages reaching 500 kV. Nowadays there is no calibration service available to proof whether the measuring system is accurate enough. The new constructions of high voltage dividers are developed in order to fulfill such requirements. One way how to reach very short response time and increase the bandwidth of voltage dividers is using of suitable liquid solutions as high voltage resistors.

The preliminary experiments with liquid high voltage resistors were performed in the High Voltage Laboratory at the Czech Technical University in Prague. Some similar experiments can be found in [14–16] however, more work in this area is needed. A verification of design and electrical parameters of various liquid solutions was at first investigated on the fast impulse voltage divider of the amplitude up to 20 kV. In the future, determined results and experiences should be used for the construction of very fast voltage divider up to 500 kV to get reference voltage divider for calibration purposes. The realized 20 kV liquid voltage divider is shown in Fig. 3.5. As the best liquid solution in term of thermal stability and frequency bandwidth, the NaCl of 5 g/l concentration was evaluated [17].

The realized liquid high voltage divider consists of liquid high voltage resistor $4k\Omega$ and low voltage resistor 2Ω . Thus, the nominal voltage ratio is 2000. The low voltage resistor is completed from five parallel SMD resistors placed in a shielded box. This solution is not ideal due to the different temperature coefficients of resistors (TCR). It is better to have the low voltage resistor as a part of the liquid resistor to have the same TCR of both parts. However, the goal of realized construction is to investigate the behavior of such voltage divider for steep impulses measurement. The long-term stability, thermal dependency and new constructions possibilities will be the subject of future work.

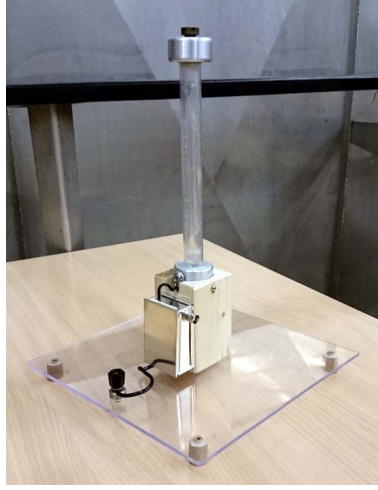


Figure 3.5: Liquid voltage divider 20 kV

The step response of liquid divider was recorded and evaluated in high voltage laboratory according to definitions described by equations (3.2) and (3.3). The input voltage was generated by step generator with amplitude 1 kV and the response was recorded by digital scope. The determined normalized step-response is shown in Fig. 3.6.

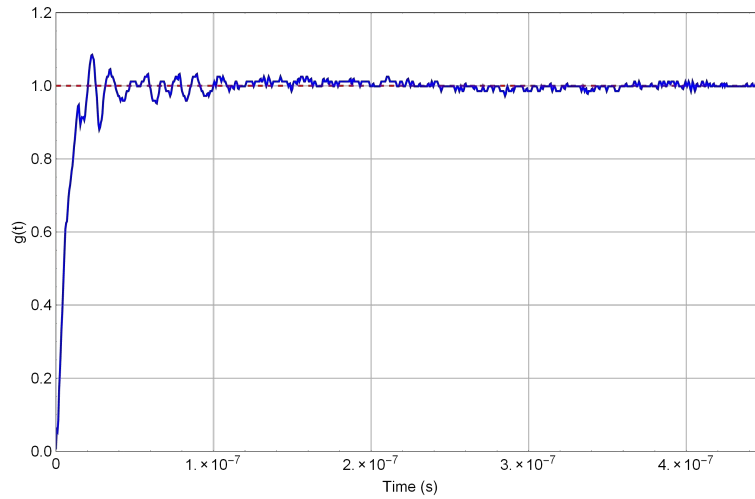


Figure 3.6: Determined step response of liquid voltage divider 20 kV

The response time $T_{ref} = 6.5 \text{ ns}$ and settling time $T_s = 120 \text{ ns}$ was evaluated from normalized step response. The maximal frequency limit is then:

$$f_m = \frac{1}{2\pi T_{ref}} = 24 \text{ MHz}. \quad (3.10)$$

The reached response time respective maximal frequency limit is roughly 10 times better than in case of common high voltage dividers and so the liquid dividers seems to be promising alternatives of ceramic discs resistors. On the other hand, the long term stability and thermal stability of divider ratio must be further investigated to approve the application for high voltage laboratory purposes.

3.2 Rogowski coils for impulse currents measurement

The Rogowski coil is a current measuring element galvanically separated from measured current. The core is usually made from a nonferromagnetic core. These two construction facts brings important technical advantages of their using, especially potentially higher frequency band, and moreover the final application of Rogowski coils in a power system measuring string is cheaper than using of current transformers. On the other hand there are some drawbacks consisting of the need to use an electronic integrator and higher sensitivity to interference fields. However for the high voltage testing purposes when the accurate current measurements of switching and atmospheric impulses and also harmonics is needed, the good properties of Rogowski coils can be very well used.

The fundamental layout of Rogowski coil is shown in Fig. 1. A measured current $i(t)$ induces an ac magnetic flux $\phi(t)$, which then induces a voltage on output terminals of sensing winding. The induced voltage can be mathematically expressed as

$$u_i(t) = N_2 \frac{d\phi}{dt} = \frac{N_1 N_2}{R_m} \frac{di(t)}{dt} = M \frac{di(t)}{dt}, \quad (3.11)$$

where N_1 is the number of turns passed by the current $i(t)$, N_2 is the number of Rc turns, R_m is the reluctance of a toroid with winding N_2 , and M is the mutual inductance between N_1 and N_2 .

When high currents are measured, one-turn winding ($N_1 = 1$) is usually used. The final waveform of the measured current is obtained by integrating the induced voltage $u_i(t)$:

$$i(t) = \frac{1}{M} \int_0^t u_i(t) dt = \frac{k_I}{M} u(t), \quad (3.12)$$

where $u(t)$ is the output voltage of the integrator, and k_I is the integrator constant.

Calibration of Rogowski coils with an integrator is usually performed at sinusoidal currents waveform $I(\omega t)$ [18–20]. The induced voltage can be expressed as

$$u_i = j\omega MI, \quad (3.13)$$

where $\omega = 2\pi f$ is the angular frequency of the measured current. When Rcs with an integrator are used for measuring current, the transfer constant of the whole system is given as

$$k_S = \frac{U_1}{I}, \quad (3.14)$$

where U_1 and I are the root-mean-square effective values of the voltage on the output of the integrator and the current passing through the central conductor.

The current source which can provide high magnitudes of currents is usually required for the calibration procedure. If the current magnitudes exceed the value of 10 kA some issues with powerful current source can arise. The required value of the calibrated current can be then generated by means of a current loop which consists of more turns passing through the calibrated Rogowski coil. This approach was studied in detail in [21]. Authors proposed a calibration circuit, see Fig. 3.7 and Fig. 3.8, in the sense of current loop with ten turns where the current passing through one turn of the loop was 3 kA. The total current of this current loop can reach the value of 100 kA.

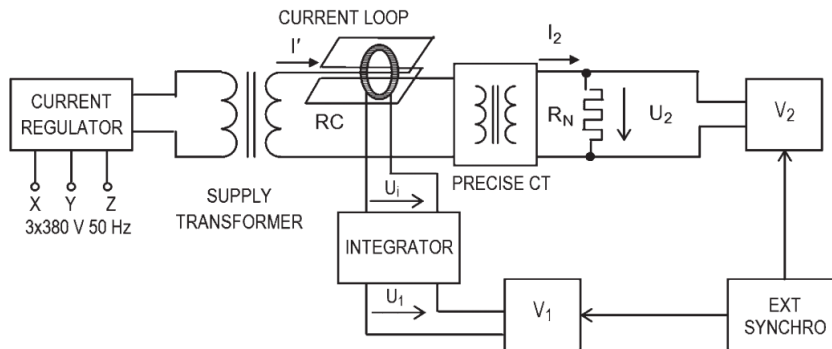


Figure 3.7: Proposed circuit with current loop for Rogowski coil calibrations [21]

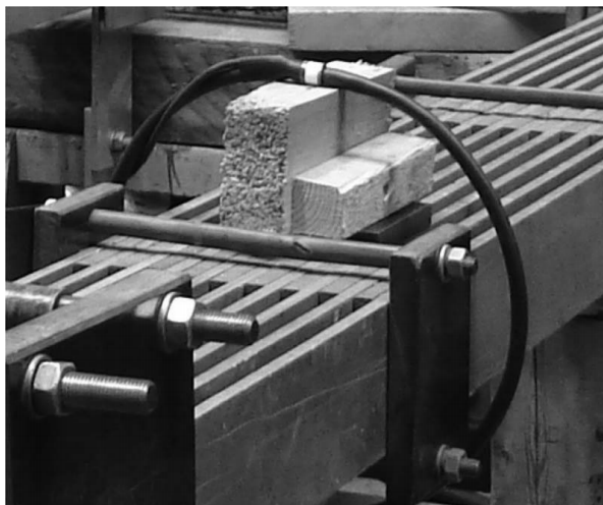


Figure 3.8: Detail of current loop with Rogowski coil [21]

The calibration current I was converted to the voltage U_2 using a Tettex 4764 standard current transformer with a standard resistor R_N as a load. The Agilent 3458A voltmeters V_1 and V_2 were used to measure the output voltage of integrator U_1 and the voltage drop U_2 on the standard resistor R_N . Both voltmeters operated in the SYNC mode to reach the highest accuracy of measured values. In advance voltmeters were simultaneously triggered in the EXT TRIG mode to eliminate the impact of fluctuation of the current I . A comparison of the calibration results using a loop of conductors and one conductor and their uncertainties shows that, for Rogowski coils, which are intended to measure very high currents, the current loop can be used for calibration purposes. The results show that the expanded uncertainty from 0.026% up to 0.035% can be achieved. These values are correct only when the systematic and random errors are neglected. The uncertainty of 0.1% is assumed for the practical on-site use.

3.2.1 Frequency dependency of Rogowski coil constant

For purposes of current impulses measurement, it is important to know the frequency dependency of Rogowski coil constant K_s . Rogowski coil parameters verification in wide frequency range was investigated in [22]. The proposed calibration circuit is shown in Fig. 3.9.

The power amplifier supplies the primary winding of the high frequency current transformer by the harmonic signal with variable amplitude and frequency. These parameters can be adjusted by the internal generator of lock-in

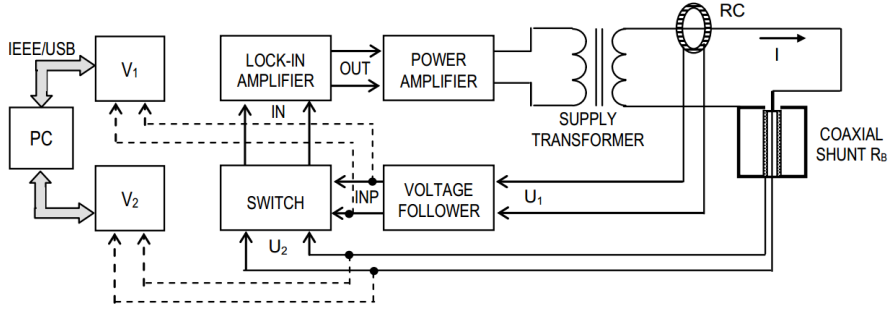


Figure 3.9: Calibration of Rogowski coil in wide frequency range

amplifier. The secondary side of transformer creates a loop which is passed through the Rogowski coil. The voltage follower is connected first to the output of Rogowski coil to eliminate an error arising from its loading. The signal from the voltage follower is then applied to the input terminals of the lock-in amplifier. The lock-in input signal can be switched to the signal from coaxial shunt R_B . The frequency dependence of K_s is then given as

$$K_s(f) = \frac{U_1(f)R_B}{U_2(f)}. \quad (3.15)$$

The values of voltages U_1 and U_2 are measured by voltmeters V_1 and V_2 which are controlled by PC through GPIB IEEE 488/USB. Usually it is preferable to express the frequency dependency of k_s as recalculated for fundamental frequency 50 Hz according to formula (3.19).

$$K_s(f) = \frac{U_1(f)R_B}{U_2(f)} \frac{50}{f}. \quad (3.16)$$

An example of determined frequency dependence of the Rogowski coil constant is shown in Fig. 3.10.

From both frequency dependencies, it is obvious, that the influence of parasitic capacitances appears. Parasitic capacitances of Rogowski coil winding result in resonance effect. It is evident that the resonance frequency of measured Rogowski coil lies close to the value 40 kHz.

Current impulses in the high voltage testing are usually close to the shape of $8/20\mu s$. The frequency spectrum of different impulses are shown in Fig. 3.11. The detailed frequency spectrum shows the maximal frequency which should be taken into consideration if the harmonics with amplitudes less than 1% of the first harmonic are neglected.

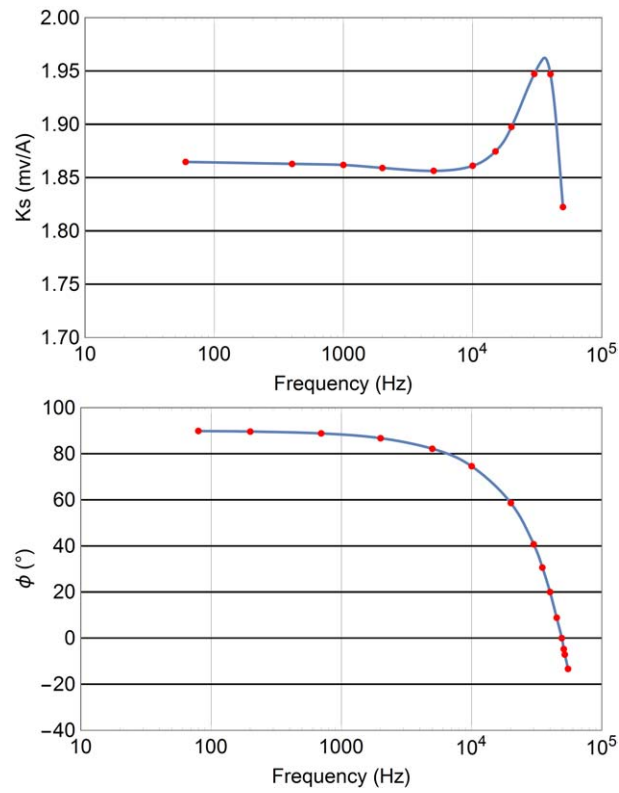


Figure 3.10: Frequency dependence of the K_s (top) and phase displacement ϕ between measured current and induced voltage (bottom)

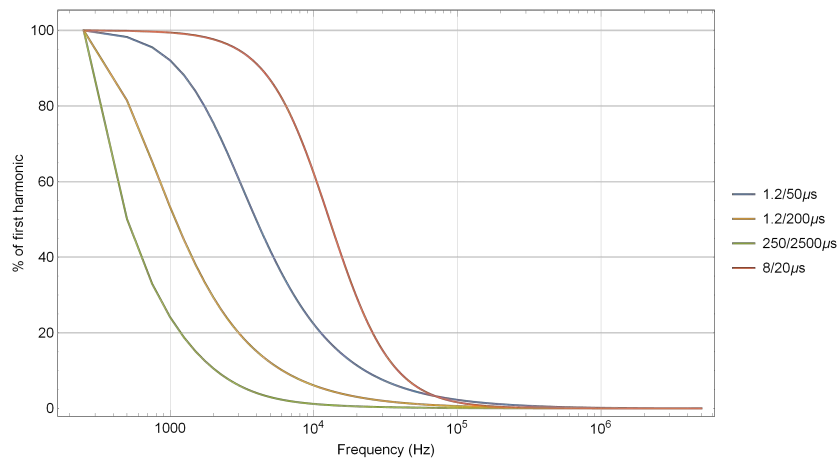


Figure 3.11: Frequency spectrum of impulses with various front time and half time

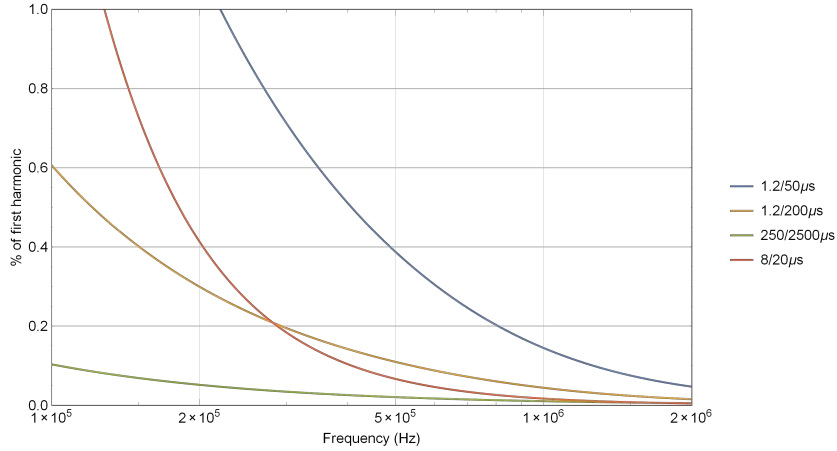


Figure 3.12: Detail of frequency spectrum of impulses with various front times and half times

If the stronger assumption of 0.1 % of the first harmonic is applied, then the maximal frequency of Rogowski coil should be at least 500 kHz to measure correctly current impulses of 8/20 μs impulse shape. The design process and developed design software for Rogowski coil with various cross-sections of sensing winding were published in [23]. The calculation of fundamental dimensions of Rogowski coil with rectangular cross-section sensing winding is based on the calculation of mutual inductance M , see equation 3.12, given by formula:

$$M = \frac{\mu_0}{2\pi} N_2 h \ln \frac{b}{a}, \quad (3.17)$$

where parameters a , b and h are described on Fig. 3.13, N_2 is the number of turns of sensing winding and μ_0 is the vacuum permeability.

Two Rogowski coils with uniformly and cross-wound sensing winding were proposed in the High voltage laboratory at Czech Technical University in Prague to measure impulse currents. Both parameters and calculated constant k_S are summarized in Table 3.1.

Computed Rogowski coil constants for power frequency (50 Hz) were verified by experimental measurement at the Czech metrology institute. The results are shown in Table 3.2.

Comparing the results shown in Table 3.2 with calculated results in Table 3.1 we can get an error up to 5 % between calculated and measured values. This error validates an approach used for the calculation of Rogowski coils constant.

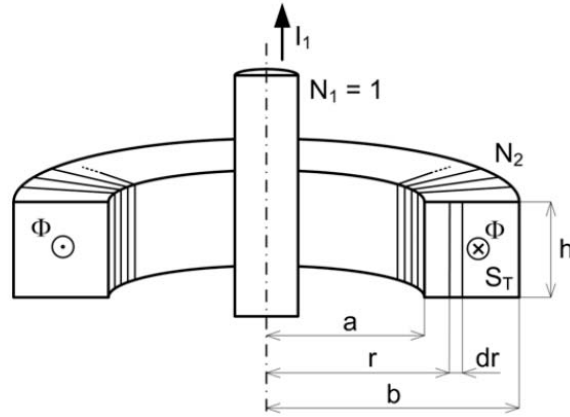


Figure 3.13: Rogowski coil with non-ferromagnetic rectangular core cross-section [23]

Parameter	RC with uniform wound winding	RC with cross wounded winding
a (mm)	89.25	89.25
b (mm)	99.25	99.25
h (mm)	24.70	24.70
d (mm)	0.16	0.3
N_2	1991	707
k_S (μH)	1.049	0.397

Table 3.1: Parameters of proposed Rogowski coils for impulse current measurement

As was mentioned above for the impulse current measurement is crucial the frequency independence of their constants at least up to 500 kHz. The parasitic inter-turn capacitance of sensing winding, winding to shield capacitance and capacitance of connecting cable causes the resonance effect. Examples of determined frequency dependencies of Rogowski coils constants are shown in Fig. 3.14 and Fig. 3.15.

Presented figures show that there is an influence of metallic shield to the resonant frequency of Rogowski coil. The applied metallic shielding decreases the highest frequency that can be measured with certain error given by characteristics in Fig. 3.12. As can be seen from Fig. 3.14 the situation is worst when the uniformly wound sensing winding with the back wire is applied. The resonance frequency is reduced by approximately 100 kHz. This reduction is caused by increasing of winding to ground capacity. In case of cross-wounded Rogowski coil, the reduction effect of resonant frequency

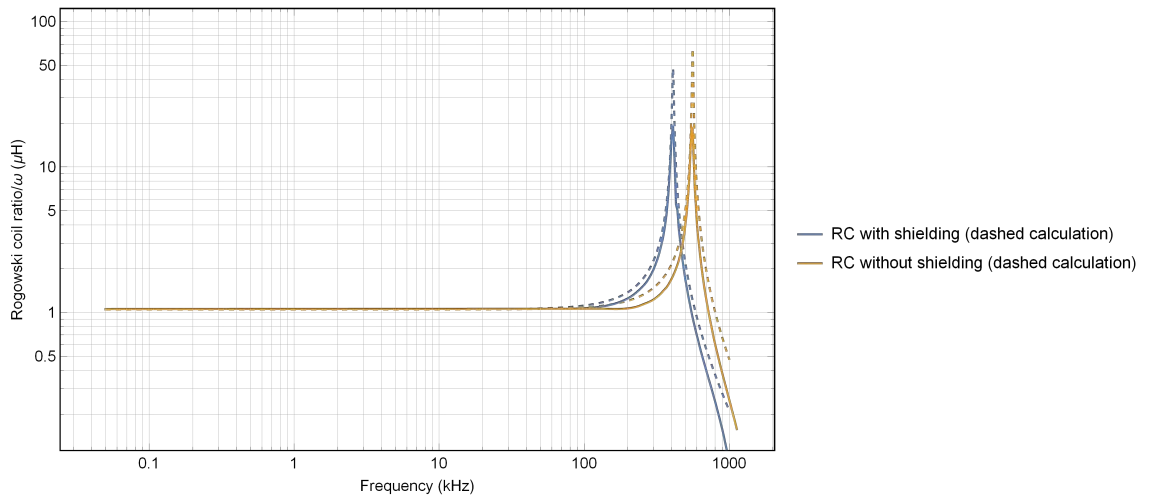


Figure 3.14: Transfer function of uniformly wound Rogowski coil

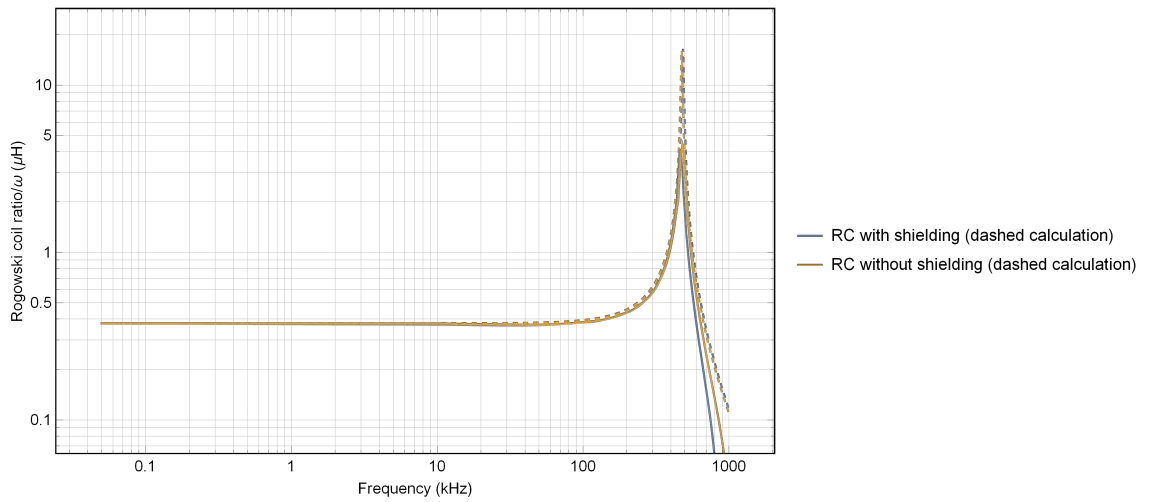


Figure 3.15: Transfer function of cross-wound Rogowski coil

	RC with uniform wounded winding	RC with cross wounded winding
k_S (μH)	0.3769	1.0608

Table 3.2: Experimentally measured constants of proposed Rogowski coils

is not so significant, because the influence of winding to ground capacity to the total capacity is not so high and prevailing influence has the capacity between the direct and reverse winding.

Frequency characteristics of Rogowski coils can be also simulated by mathematical models. A first approximation can be reached by equivalent model with lumped parameters shown in Fig. 3.16, where $I(t)$ is the measured current, M is the mutual inductance and R_C , L_C are coil resistance and self-inductance and C_C is the coil total (inter-turn and coil to ground) capacitance and R_L is the load resistance.

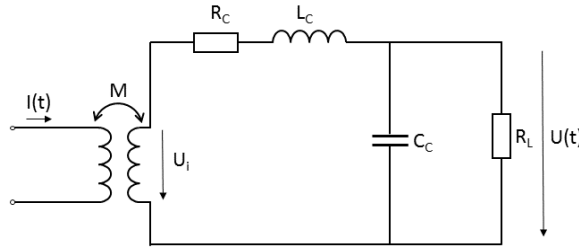


Figure 3.16: Rogowski coil lumped parameter equivalent circuit

The lumped model's transfer function $G(j\omega)$ can be derived from equations:

$$\begin{aligned}
 -j\omega MI + R_C I_i + j\omega L_C I_i + U_t &= 0, \\
 I_i &= \left(\frac{1}{R_C} + j\omega C_C \right) U
 \end{aligned} \tag{3.18}$$

in the form of

$$G(j\omega) = \frac{j\omega M}{-\omega^2 L_C C_C + j\omega \left(C_C R_C + \frac{L_C}{R_L} \right) + \left(\frac{R_C}{R_L} + 1 \right)}. \tag{3.19}$$

The mutual inductance for the rectangular cross-section can be calculated according to 3.17. The conventional calculation method of self-inductance usually only take into account the main magnetic flux, ignoring the impact of the leakage inductance. The leakage flux is present in the Rogowski coils with the smaller number of turns. The flux is not fully enclosed in the toroid, and

there is some flux around the individual turns. The leakage inductance L_σ is approximated as a circular conductor at the distance H from the ground plane, thus:

$$L_\sigma = \frac{\mu_0 l_w}{2\pi} \ln \left(\frac{2H}{kr_w} \right), \quad (3.20)$$

where l_w is the length of the windings wire, H is the distance between coil and shield, r_w is the winding wire radius, k is radius correction factor taking account of the thickness of the winding wire insulation. The self-inductance of the Rogowski coil is modeled as the inductance of an ideal toroid:

$$L_S = \frac{\mu_0 h N^2}{2\pi} \ln \left(\frac{b}{a} \right), \quad (3.21)$$

where N is the number of windings turns. The total self inductance of Rogowski coil can be described as the sum of self and leakage inductance:

$$L_T = L_S + L_\sigma. \quad (3.22)$$

The distributed stray capacitance between the winding and the shield is usually also approximated as a circular conductor at the distance H from the ground plane, i.e.

$$C_S = \frac{2\pi\epsilon_0 l_S}{\ln \left(\frac{2H}{r_w} \right) l_w}, \quad (3.23)$$

where $l_S = l_w - Nh$. The inter-turn stray capacitance C_{IT} is usually neglected for pure theoretical simulations. However, it is possible to estimate it from the measurements of the Rogowski coil impedance or from the resonance frequency since the accurate calculation is difficult.

The electrical parameters for both designed Rogowski coils used for the model with lumped parameters and resulted resonant frequencies are presented in Table 3.3.

The comparison of calculated and measured transfer functions are shown in Fig. 3.14 and Fig. 3.15. The presented model with lumped parameters is sufficient enough to provide resonant frequencies of Rogowski coils and determine their bandwidth.

3.2.2 Influence of Rogowski coil homogeneity to the measurement accuracy

The Rogowski coil homogeneity is a quality parameter which has the direct impact on the measurement error. Imagine a long coil with a few turns which

	Uniform wounded winding		Cross wounded winding	
	Without shielding	With shielding	Without shielding	With shielding
$L_C(mH)$	2.08	2.08	0.282	0.281
$R_C(\Omega)$	119	119	24	24
$C_C(pF)$	38.5	71.8	381.9	398.1
$f_r(kHz)$	560	410	485	475
$M(\mu H)$	1.049	1.049	0.397	0.397

Table 3.3: Electrical parameters of proposed Rogowski coils

creates dipole magnetic field when the current flowing through. The coil is placed in the middle of the Rogowski coil. In an ideal case, when the sensing winding is homogenous, the integral of the magnetic field along a closed loop representing the mean path in the middle of sensing winding is zero. It means that the output voltage is zero as well. Real constructions of Rogowski coils have non-uniformly wounded winding (mostly in the place of outputs connectors) and slightly variable cross section. Then, the resulting output voltage is not equal to the zero. The value of output voltage is a function of angle of dipole field rotation which is generated by the coil. The example of homogeneity measurement test set-up, realized at Czech Metrology Institute, is shown in Fig. 3.17.

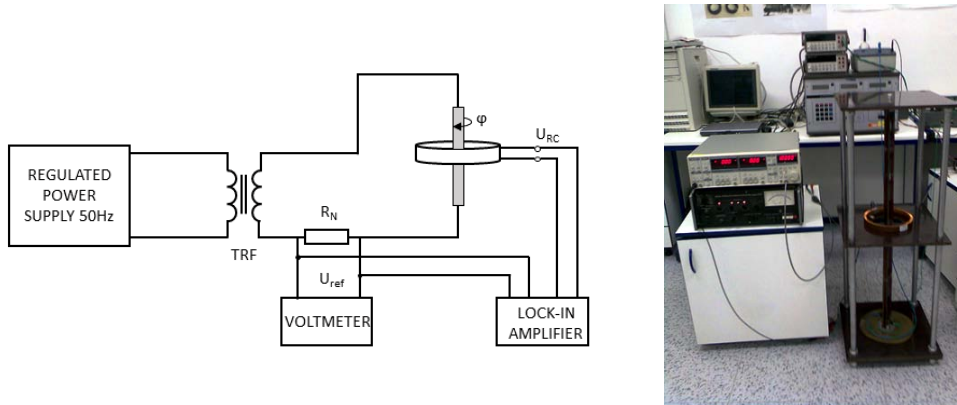


Figure 3.17: Homogeneity measurement test set-up (left) and realization of measurement at the Czech Metrology Institute (right)

Figure 3.18 shows typical graphs of homogeneity measurements. As can be seen from Fig. 3.18 the Rogowski coil with cross wounded winding has higher amplitude of induced voltage. Assuming the same geometrical dimensions of both tested coils the crossing of winding turns brings worst homo-

generality compare to uniformly wounded winding. This effect decreases the accuracy of coil in cases when the wire with measured current is not placed exactly in the center of toroid.

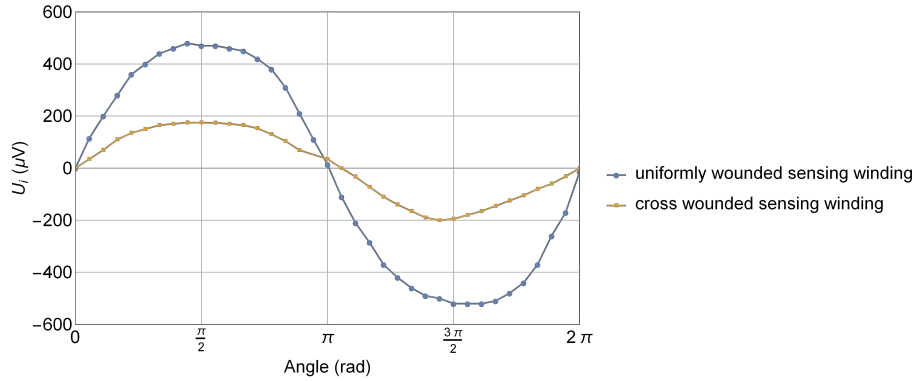


Figure 3.18: Output voltage of Rogowski coils at uniformity measurement

3.2.3 Influence of Rogowski coil shielding to the measurement accuracy

As the Rogowski coils are very sensitive to electrostatic interference, the metallic shielding of Rogowski coils is necessary. The metallic shield must be appropriately split not to create a short circuit turn. The testing of electrostatic shielding efficiency is an important tool for the Rogowski coil design which requires special approaches and test setups.

The proposal of the test set-up which was realized in the High Voltage Laboratory of Czech Technical University in Prague is shown in Fig. 3.19 and Fig. 3.20.

The test configuration consists of an aluminum plate electrode on which the insulating pad and tested Rogowski coil are placed. The impulse $1.2/50 \mu s$ is applied to the plate electrode. The applied impulse voltage and output voltage of Rogowski coil is recorded by digital scope. The test is performed for the horizontal and vertical arrangement of Rogowski coil and for the cases when the shielding is present and when the shielding is removed to investigate how is the change of output voltage measured by Rogowski coil.

The peak values and rms values are then calculated to determine shielding efficiency of tested Rogowski coils. In Table 3.4 and Table 3.5 are summarized examples for two tested Rogowski coils described in previous chapter.

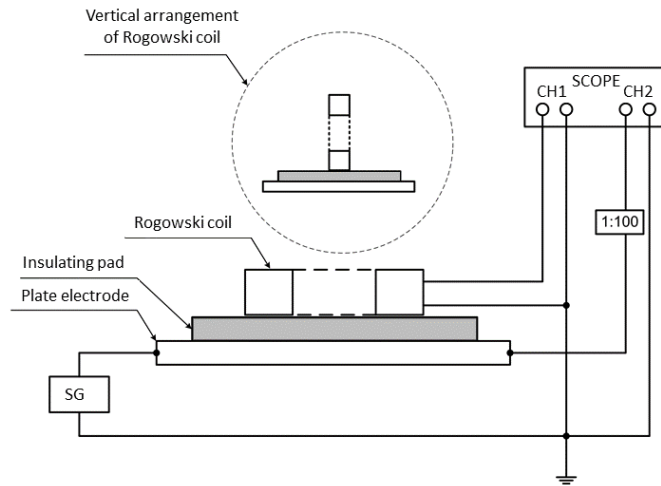


Figure 3.19: Shielding efficiency test set-up - without shielding

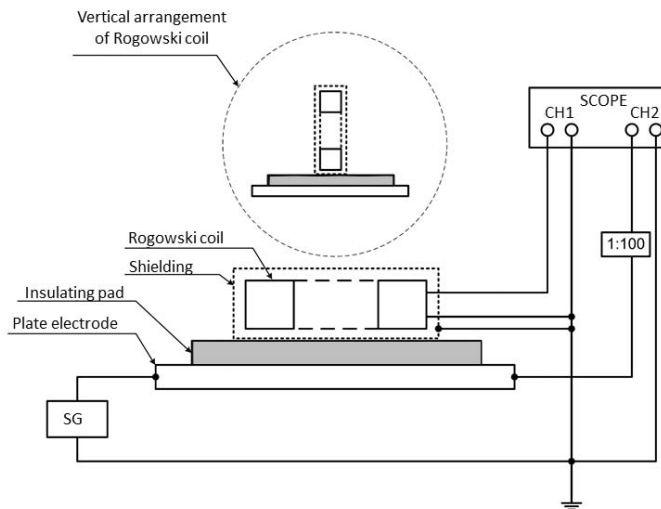


Figure 3.20: Shielding efficiency test set-up - with shielding installed

Rogowski coil configuration	Peak value (V)	RMS value (V)
Vertical arrangement, no shielding	93.6	134.7
Vertical arrangement, shielding	19.4	0.7
Percentage of reduction (%)	79.3	99.5
Horizontal arrangement, no shielding	125.8	492.6
Horizontal arrangement, shielding	10.2	0.3
Percentage of reduction (%)	91.9	99.9

Table 3.4: Determined shielding efficiency of Rogowski coil with uniformly wounded winding

Rogowski coil configuration	Peak value (V)	RMS value (V)
Vertical arrangement, no shielding	39.4	8.5
Vertical arrangement, shielding	7.7	0.2
Percentage of reduction (%)	80.5	97.6
Horizontal arrangement, no shielding	69.9	17.6
Horizontal arrangement, shielding	9.9	0.3
Percentage of reduction (%)	85.8	98.3

Table 3.5: Determined shielding efficiency of Rogowski coil with cross-wounded winding

3.3 Using of nanocrystalline material for impulse current and voltage measurement

Common instrument transformers can not be used to impulse current and voltage measurement due to their frequency limit (approximately 10 kHz) when the losses of ferromagnetic steels are significantly increasing, see Fig.3.21. The using of ferrite cores brings another issues with the application in power engineering because of their low saturation flux. With the development of nano materials and technology the commercial companies starts to provide various magnetic materials based on nanocrystalline alloys. The nanocrystalline alloys are materials on the basis of Fe, Si and B with additions of Nb and Cu produced by Rapid Solidification Technology. Thin ribbons are initially in the amorphous state and then are crystallized by heat treatment of 500 – 600°C. This process leads to grained microstructure with the grain size of 10 nm.

These nanocrystalline alloys evince high magnetic permeability, high magnetic flux densities, and good thermal stability.

The obvious disadvantage of a nanocrystalline material is very high fragility and difficult machinability. The production of cut cores requires sophisti-

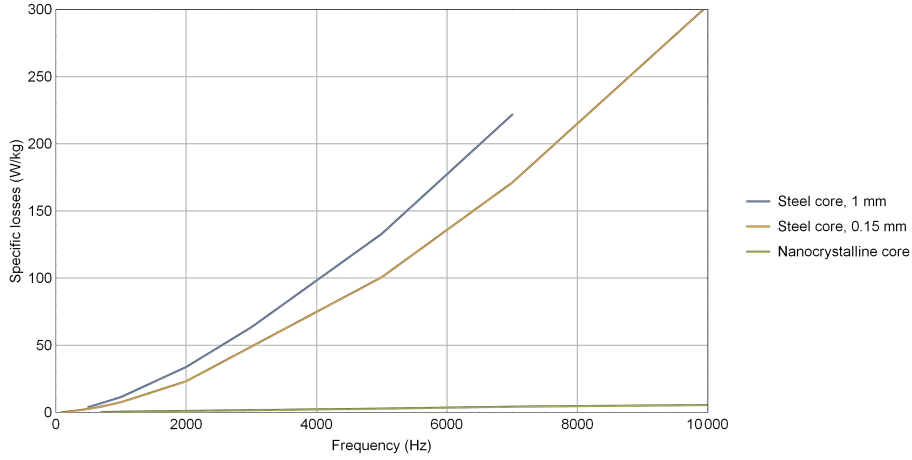


Figure 3.21: Comparison of specific losses of magnetic C-cut cores made from steel with thickness of plates 1 mm, steel with thickness of plates 0.15 mm and nanocrystalline alloy

cated approaches which always significantly reduce magnetic properties of cores. Thus, the using of full toroidal magnetic cores is preferred as much as possible. In the case of current transformers, the using of full toroidal cores can be an issue because sometimes the flexible design is required, and the magnetic core must be split. For the instrument voltage transformers is usually the main problem the higher number of turns and higher required dielectric strength. Coils are usually first wounded on the frames and then they are pushed on the split core. The direct winding on toroidal coils is either difficult or sometime even impossible.

3.3.1 Frequency properties of nanocrystalline magnetic cores

From the equivalent circuit of transformer and its vector diagram, we can very easily express the well-known theoretical formulas for calculating the current ratio error ϵ_I and the phase angle error φ_I in the form:

$$\epsilon_I = -\frac{Bl}{\mu_0\mu_a NI} \sin(\delta + \psi), \quad (3.24)$$

$$\varphi_I = -\frac{Bl}{\mu_0\mu_a NI} \cos(\delta + \psi), \quad (3.25)$$

where B is the magnetic induction of the fundamental harmonic, l is the mean magnetic path, μ_0 is the magnetic constant, μ_a and δ are apparent permeability

and loss angle of the magnetic core corresponding to the induction B . The angle ψ is given by the phase shift on the burden. In the case of the real burden $\psi = 0$. The equation (3.25) is simplified assuming that for the small error angle between the primary and secondary currents the $\varphi_I \approx \tan \varphi_I$. Similar error formulas can be derived for a voltage transformer. Assuming the transformer is not loaded and the secondary current I_2 is equal to zero the errors formulas can be expressed as:

$$\epsilon_U = \frac{|\mathbf{U}'_2| - |\mathbf{U}_1|}{|\mathbf{U}_1|} = \frac{|\mathbf{Z}_{\sigma 1}|}{|\mathbf{Z}_{\sigma 1} + \mathbf{Z}_m|} - 1, \quad (3.26)$$

$$\varphi_U = \arg \left[\frac{\mathbf{U}'_2}{\mathbf{U}_1} \right] = \arg \left[\frac{\mathbf{Z}_{\sigma 1}}{\mathbf{Z}_{\sigma 1} + \mathbf{Z}_m} \right], \quad (3.27)$$

where \mathbf{Z}_m is the main impedance and $\mathbf{Z}_{\sigma 1}$ is the impedance of primary side regarding the transformer equivalent diagram. Evidently,

$$\mathbf{Z}_m = \frac{\omega L_m R_m}{\omega^2 L_m R_m C_m - j\omega L_m - R_m} \quad (3.28)$$

and

$$\mathbf{Z}_{\sigma 1} = R_{\sigma 1} + j\omega L_{\sigma}, \quad (3.29)$$

where L_m , R_m , C_m are the main inductance, resistance and capacitance, $R_{\sigma 1}$ is resistance of primary winding and $L_{\sigma 1}$ is the leakage inductance of primary winding. The main inductance L_m and the main resistance R_m can be expressed as:

$$L_m = \frac{N_1^2 \mu_0 S \mu_a}{l \mu'}, \quad (3.30)$$

$$R_m = \frac{\omega N_1^2 \mu_0 S \mu_a}{l \mu''}, \quad (3.31)$$

where l is the mean magnetic path length of magnetic flux, N_1 is the number of turns on the primary side of the transformer, S is the cross section of the magnetic core. The apparent permeability μ_a is defined as $\mu_a = \sqrt{\mu'^2 + \mu''^2}$ where μ' and μ'' are the real and the imaginary components of complex permeability. For the simplification the influence of the main capacitance is neglected, see [24, 25] for a more detailed explanation.

As can be seen from equations (3.26) - (3.31), measurement errors are given by the dependence of the apparent permeability and both components

of the complex permeability on the frequency and the magnetic induction. The knowledge of frequency dependency of complex permeability of used magnetic material is crucial for the designing of transformers which are intended for measurement of impulse waveforms or harmonics components.

Frequency dependences of apparent permeability μ_a and loss angle δ can be measured in accordance with the circuit shown in Fig. 3.22, published in [26].

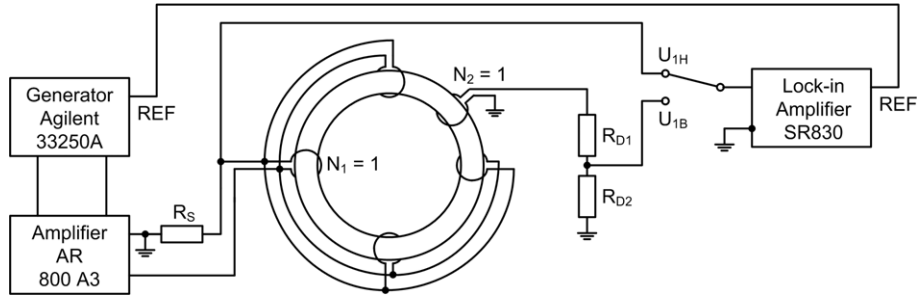


Figure 3.22: Apparent permeability and loss angle measurement

The maximum value for magnetic induction of the fundamental harmonic frequency can be expressed as

$$B_{1m} = \frac{U_{1B} \left(1 + \frac{R_{D1}}{R_{D2}} \right)}{4.44 f S N_2}, \quad (3.32)$$

where U_{1B} is the effective value of the fundamental harmonic frequency of the induced voltage in the transformer winding with N_2 turns that is measured on the resistive voltage divider with ratio $\frac{R_{D1}}{R_{D2}}$. The maximum value for the magnetic field intensity of the fundamental harmonic frequency is given as

$$H_{1m} = \frac{\sqrt{2} U_{1H} N_1}{l R_S}, \quad (3.33)$$

where U_{1H} is the effective value of the fundamental harmonic frequency voltage on the coaxial shunt R_S , l is the mean magnetic path, N_1 is number of turns on primary side of transformer. The loss angle of the ferromagnetic core is defined as

$$\delta = 90 - (\phi_{1B} - \phi_{1H}), \quad (3.34)$$

where ϕ_{1B} and ϕ_{1H} are phase shifts related to the reference voltage REF from generator. These phase shifts are measured by lock-in amplifier. The

detailed description of measuring approach for specific impulse current transformer can be found in [26].

The measured dependence of the maximum sinusoidal magnetic induction on the magnetic field intensity for different frequencies is shown in Fig. 3.23. The composition of measured nanocrystalline alloy is $Fe_{73}Cu_1Nb_3Si_{16}B_7$. This dependency shows that the optimal value for maximum induction used for the design of the transformer could be roughly 0.6 T for the measured frequency range up to 40 kHz.

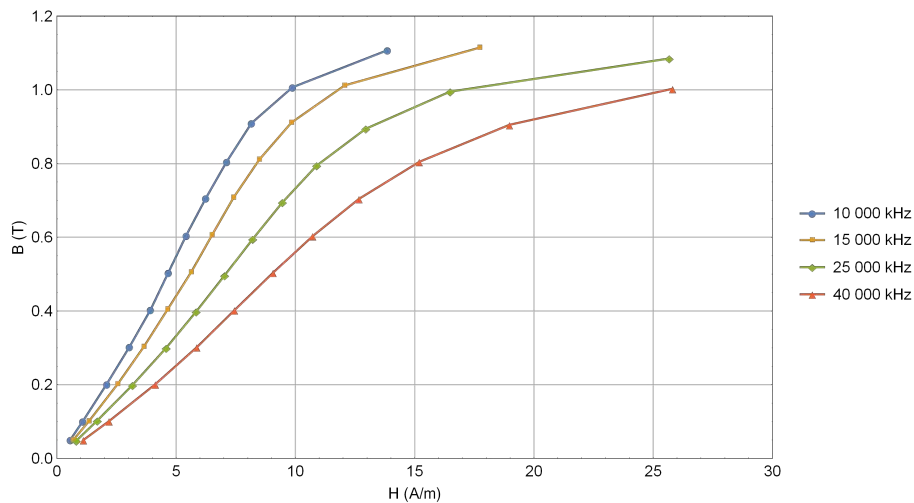


Figure 3.23: Magnetic induction dependence on the magnetic field intensity for various frequencies

Similar conclusions can be deduced from the measured dependence of the apparent permeability and the loss angle on the magnetic induction for different frequencies, see Fig. 3.24 and Fig. 3.25.

Only to see the overall view of the behavior of magnetic properties of the nanocrystalline material depending on frequency the 3D graph with all three parameters is presented in Fig. 3.26.

3.3.2 The application of nanocrystalline magnetic core for impulse current measurement

An example of proposal and realization of the current transformer is very well described in [26]. Due to the specific application in photovoltaic power plants, where the currents of high voltage inverters need to be measured, the proposed current transformer has magnetic induction 0.2 T and real burden 200 VA and given ratio 1:1. The values for apparent permeability and loss

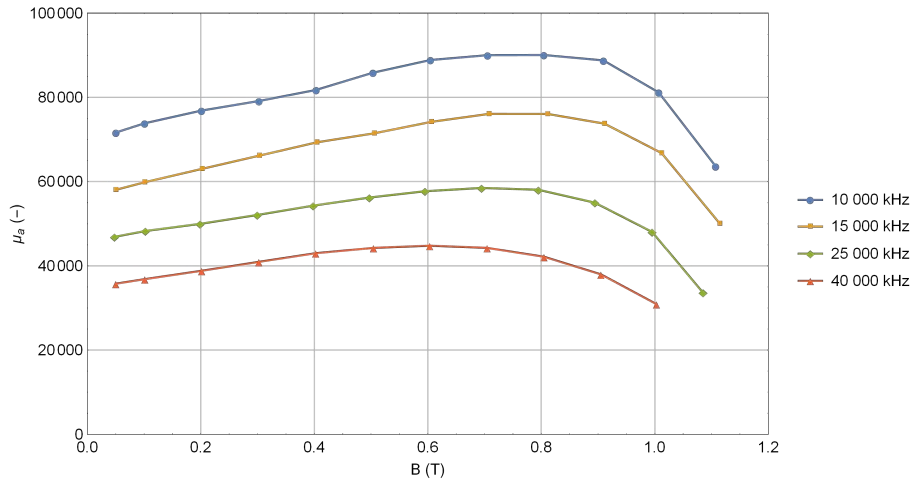


Figure 3.24: Dependence of the apparent permeability on the magnetic induction for various frequencies

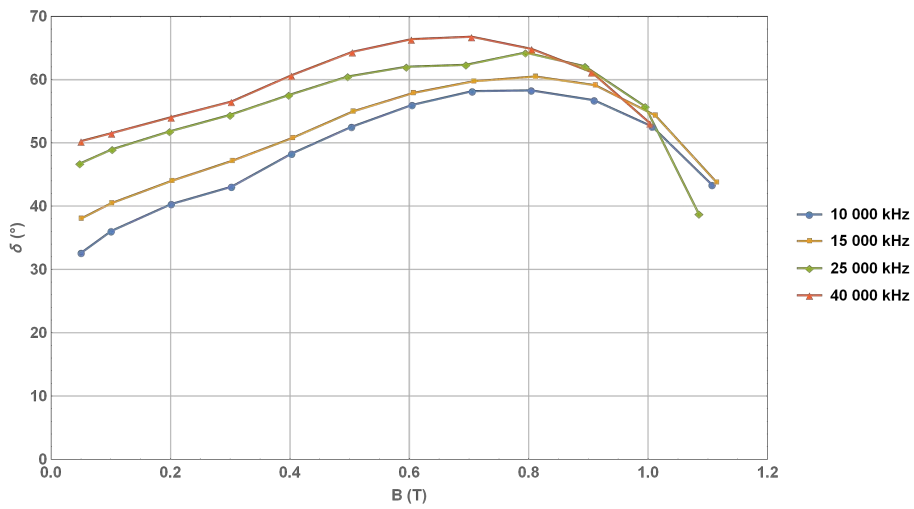


Figure 3.25: Dependence of the loss angle on the magnetic induction for various frequencies

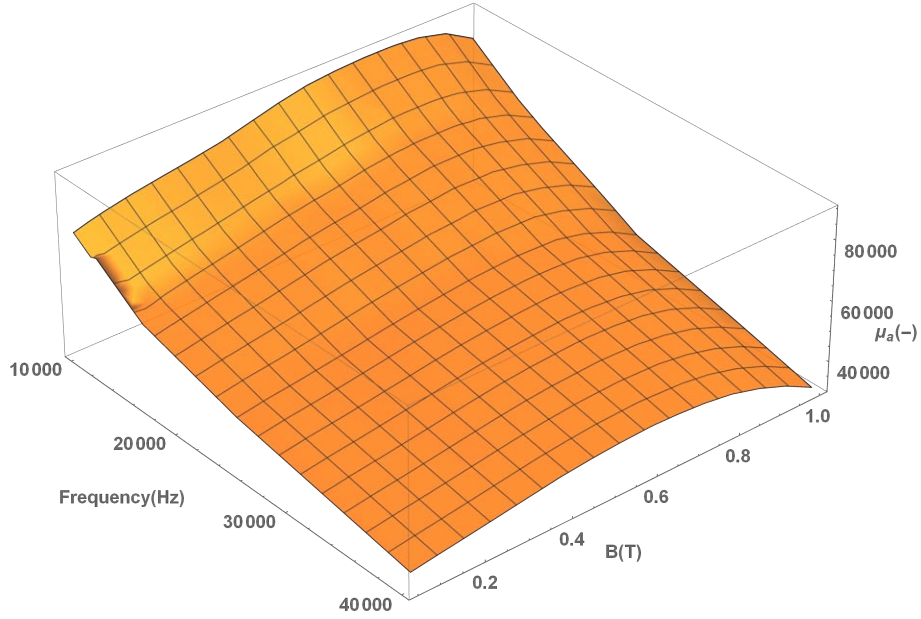


Figure 3.26: Apparent permeability dependence on the frequency and magnetic induction

angle were read for fundamental frequency 25 kHz from the graphs in Fig. 3.24 and Fig. 3.25. Finally, the current and angle errors were calculated using formulas (3.24) and (3.25). The resulting current ratio error value is $\epsilon_I = -2.7\%$, and the phase angle error $\delta = 1.7^\circ$.

A final verification of the proposed CT can be performed for a square current waveform with fundamental frequency 25 kHz. The transformer primary winding is powered by a current with the waveform shown in Fig. 3.27. The secondary winding was connected to the rated real burden 200 VA. The currents are measured by coaxial shunts with proven frequency independence up to 1 MHz.

The calculation of the current error directly from measured current waveforms must follow the definition of the total current error in the form

$$\epsilon_c = \frac{100}{I_1} \sqrt{\frac{1}{T} \int_0^T (pi_s - i_p)^2 dt}, \quad (3.35)$$

where p is the transformer ratio, I_1 is the rms value of the primary current, T is the signal period, i_p and i_s are instantaneous values of primary and secondary current.

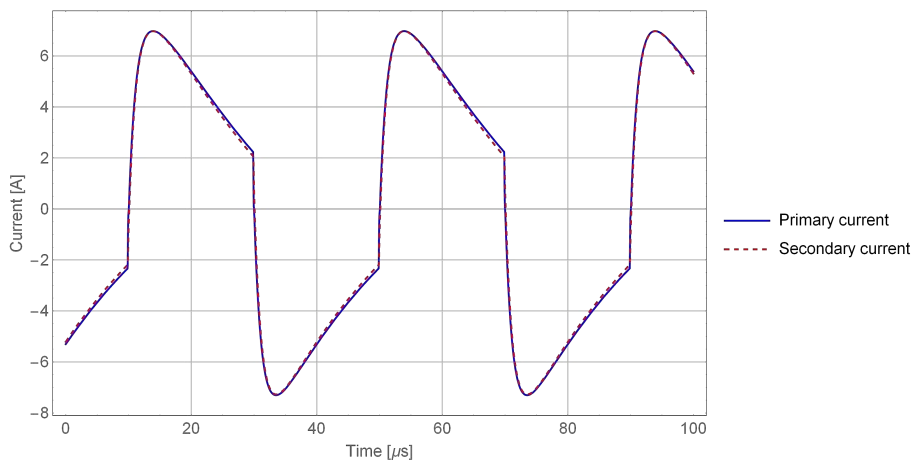


Figure 3.27: Primary and secondary current waveforms

There may not be an exact definition of the angle error for impulse currents. It is assumed that this error will be related to the time shift of the primary and secondary currents, see Fig. 3.28. Then the angle error can be determined from the interpolation of current samples in the proximity of the signal zero-crossing. The acquired time differences are very small. It is necessary to involve a suitable interpolation of samples, i.e. the higher order spline interpolation. The determined time differences of zero crossing points are, after the conversion into angular units, directly equal to the angle error.

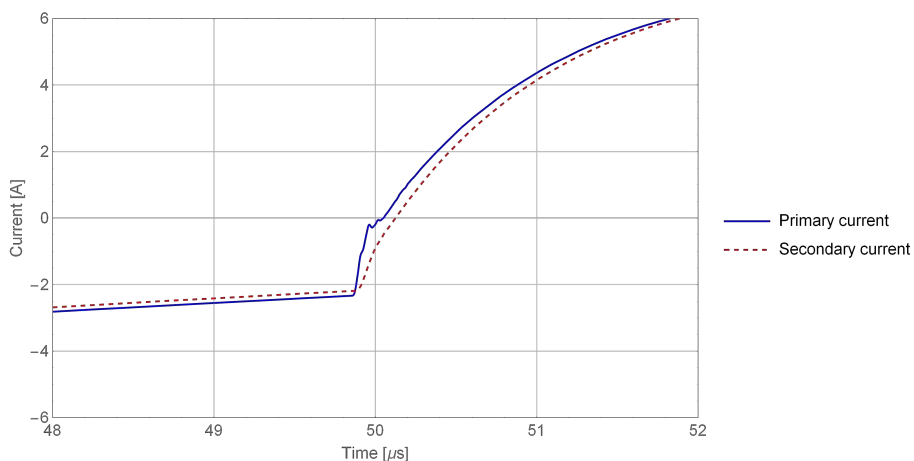


Figure 3.28: Primary and secondary current waveforms detail of zero-crossing

The total current error was determined by applying the procedures de-

scribed here to the measured square current waveform, and the time shift between the zero-crossing of the primary and secondary current corresponds to an angle of 0.80° . These values are in correspondence with errors determined in the transformer proposal process.

Chapter 4

The Flashover process in long air gaps

4.1 Streamer Breakdown

One of the first theory of electrical breakdown in the air was first introduced by Townsend at the beginning of the twentieth century. Spark breakdown consists of primary and secondary processes when the primary process is described as a multiplication of electrons by electron impact ionization mechanism. A single electron traveling the length d creates $e^{\alpha d}$ free electrons. The coefficient α is usually called as first Townsend coefficient and depends on the electrical field intensity E and pressure p . The product of $e^{\alpha d}$ electrons was called an electron avalanche. The secondary process involves another source of initiating electrons. These electrons are released from cathode as a consequence of positive ions bombardment and photoelectric effect when the short wavelength photons impact on a cathode. This process is quantified by second Townsend coefficient γ that express how many electrons are released after one positive ion hits the cathode. Under these conditions, Townsend and Thompson have derived the well-known formula for the observed current in the form

$$i = i_0 \frac{e^{\alpha d}}{1 - \gamma(1 - e^{\alpha d})}. \quad (4.1)$$

As can be seen from (4.1) for $\gamma e^{\alpha d} < 1$ the current depends on i_0 and is not self-sustained. For $\gamma e^{\alpha d} = 1$ each electron from the primary process is multiplied by γ that is large enough to produce one secondary electron. This condition is the threshold for self-sustained discharge, independent of i_0 . The Townsend spark mechanism can be shortly described as follows:

1. Since $\gamma e^{\alpha d} \geq 1$ one of the initiating electrons creates electron avalanche along the gap at an approximate speed 10^7 cm/s.
2. All electrons are absorbed by the anode and positive ions start to move towards the cathode with an approximate speed 10^5 cm/s.
3. $\gamma e^{\alpha d} \geq 1$ new electrons are released from cathode and $\gamma e^{\alpha d} \geq 1$ new avalanches are established.
4. The point 3 is continuously repeated when after the k sequences the amount of $\gamma^{k-1} e^{k\alpha d} \geq 1$ positive ions is produced and the self-sustained glow or arc is then achieved.

The investigations revealed in the coming years that there is a contradiction between the Townsend theory and experimentally determined reality. For example, it was discovered that the observed formation time lag (1 cm sparks, atmospheric pressure) in the order of 10^{-7} s is not comparable with 10^{-5} s determined from the Townsend theory. These difficulties led to the development of new theory, presented by Meek and Loeb in 1940 and called the streamer theory [27, 28]. The streamer theory is an extension of the Townsend theory when the field distortion by space charge and photoelectric ionization are taken into account. In this theory, an electron avalanche grows across the gap to the anode, leaving the slow positive ions behind. The positive space charge density seriously distorts the imposed electrical field. Electrons created near the cathode by photoionization process are accelerated towards this positive space charge with high intensity and creates new avalanches. Due to the higher electric intensity and the higher value of α coefficient the tip of positive charge will be extended closer to the cathode. The electrons are moving in opposite direction than streamer tip contributing to the acceleration of the whole process. Streamers can be then characterized as weakly luminous channels with intensive ionization at their tips and almost neutral channel behind. Two zones can be recognized: active zone characterized by space around the tip and passive zone characterized by a low conductive channel between the tip and electrode. The detailed description of the streamer structure can be found in [29]. In 1939 Raether, published his streamer breakdown criterion that the more likely formation of streamer occurs when the avalanche gain reaches the value of 10^8 [30]. This criterion was derived from the balance of electrical field at the head of an avalanche and the applied electrical field.

4.2 Streamer propagation

The physical and experimental background of streamer-leader propagation for a long air gap was intensively studied by many investigators in the eighties and nineties of the last century [31–36]. It was found that the discharge development consists of several phases, see Fig.4.1.

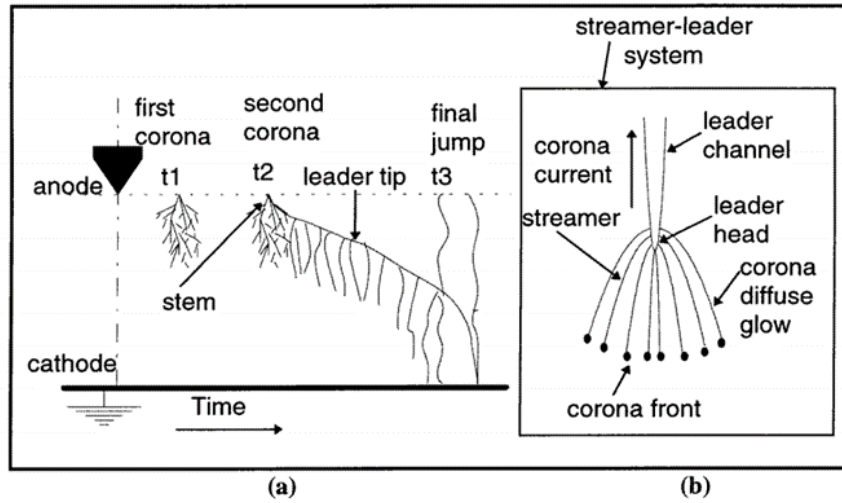


Figure 4.1: Streamer - leader process for long gap configuration [37]

At the beginning when the applied voltage is increasing, the discharge process is initiated by the formation of the first corona which is usually described as a luminous branched filaments - streamers. As it was mentioned before, the criterion for streamer development is given by the critical gain 10^8 of ions at the head of an avalanche. The condition for streamer inception and propagation can be formulated as:

$$e^{\int_0^{x_s} (\alpha - \eta) dx} > N_{stab}, \quad (4.2)$$

where x_s is the length of streamer, α is the ionization coefficient, η is ion attachment coefficient, and N_{stab} is a minimum of charge at which the streamer is stable. In Fig. 4.2 is shown the distribution of the ion charge along the streamer path as a result of the simulation model. It can be seen that the number of ions is increasing in the high field region up to the maximum and then decreasing until the streamer propagation stops. The maximum is reached at applied field approximately 6.8 kV/cm.

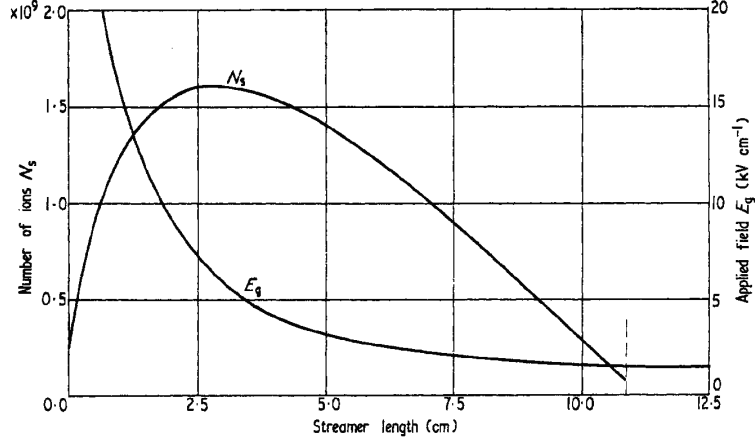


Figure 4.2: Distribution of the number of positive ions and applied field along the streamer (150 cm gap, 123 kV inception voltage) [31]

Bondiou and Gallimberti introduced in [38] a model for the calculation of the number of positive ions in the streamer head as:

$$N(x) = \frac{2eR + \mu}{4a} \left(V_0 + \frac{4a}{2eR + \mu} N_0 - \frac{\beta}{2eR + \mu} x - V(x) \right), \quad (4.3)$$

where R is the radius of streamer head, V_0 is the potential in $x = 0$, N_0 is the number of positive ions in $x = 0$, $V(x)$ is the potential distribution along x-direction and $a = \frac{0.4e^2}{4\pi\epsilon_0}$. Coefficients μ and β represents loss and gain of energy.

The streamer stability condition can be then expressed as:

$$E(x) = \frac{\beta}{2eR + \mu}. \quad (4.4)$$

As can be seen from equation (4.4) the stability condition of streamer propagation depends on the coefficients β and μ and the streamer head radius R . The authors determined the stability field values for both polarities $E_{s+} \approx 500 \text{ kV/m}$ and $E_{s-} \approx 750 \text{ kV/m}$ which is consistent with the experimental observations. These values can be used for simplified calculations of the streamer extension. The streamer length is directly given by the geometrical arrangement if the constant stability field along the streamer extension is assumed. The total streamer space charge is calculated using this equation:

$$\Delta Q = 4\pi k\epsilon_0 \int_0^{x_s} u(t_1, x) - u(t_2, x) dx, \quad (4.5)$$

where k is a geometric factor and $u(t_1, x) - u(t_2, x)$ expresses the potential change in the streamer region. When the total space charge in streamer region reaches the value of approximately $1 \mu C$ [39] the streamer is transformed to the leader channel. The simplified model for k factor calculation can be found in the appendix of [37]. The N parallel streamer filaments with the length l are assumed in this model. The distance of filaments from the central filament is assigned as a_i and the same charge distribution along a streamer filaments is assumed. Then the k factor can be expressed as:

$$k = \frac{N}{\ln\left(\frac{l+\sqrt{l^2+a^2}}{a}\right) + \sum_{i=1}^{N-1} \ln\left(\frac{l+\sqrt{l^2+a_i^2}}{a_i}\right)}. \quad (4.6)$$

For the short distances, streamer can directly bridge the gap between electrodes and after that the flashover occurs. In case of longer gaps the leader propagation phenomena will start.

4.3 Leader channel formation and advancement

The new structure called leader is created after the streamer channel is established. This transition is accompanied by a temperature increasing from approximately 300 K to 1000-1200 K. This energy gain leads to the many effects which drastically increase the conductivity of the stem and the electric field at its tip. The higher electric field generates the second streamer corona and the leader advancement process. The leader channel is formed as a thin luminous channel, connecting the corona zone to the high voltage electrode. The leader channel diameter (0.5 - 1 mm for 1.5 m gap) depends on total charge flowed through the leader. The injected current induces the Joule heating of the gas in front of the leader's head and the conductivity increases. The leader's head is moving towards the opposite electrode when the axial velocity has a random fluctuation. The effective value of velocity is proportional to the current I_l

$$v_l = \frac{I_l}{q_l}, \quad (4.7)$$

when the constant q_l represents the charge needed for a unit length leader advancement. The required charge depends on many factors. The measured and theoretically calculated dependency of q_l on absolute humidity for different impulse durations is shown in Fig. 4.3

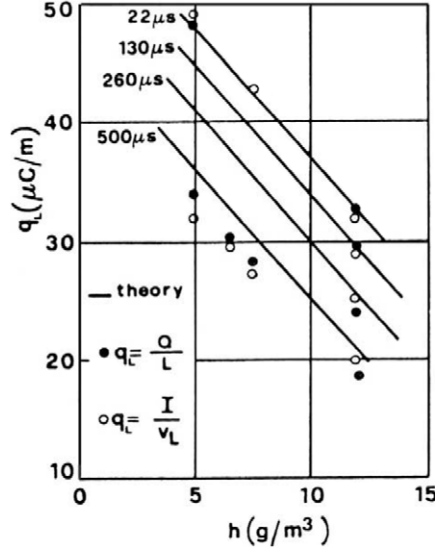


Figure 4.3: Calculated and experimentally measured values of charge per unit length as absolute humidity dependence for different impulse front times) [40]

As can be seen the q_l achieves the values from $20 \mu\text{s}/\text{cm}$ to $50 \mu\text{s}/\text{cm}$ within the relative humidity 30-70 % at normal pressure and temperature. The more detailed theoretical derivations and formulas were published in [40].

These processes expand the channel and modify the internal electric field. As the leader approaches the final jump the electric field distortion due to leader space charge starts to play a decisive role. The different equations and numerical models have been introduced to simulate leader channel inception voltage and advancement. The models based on physical description have been validated mainly with experimental measurement of Les Renardières' Group. A model presented by Rizk [41–43] is often used for engineering simulations as more practical and representative. This model provides expression of continuous leader inception voltage and breakdown voltage for different rod-plane gaps. The Rizk's expression for continuous leader inception voltage has a form of:

$$V_{lc} = \frac{V_{c\infty}}{1 + \frac{A}{R}}, \quad (4.8)$$

where $V_{c\infty}$ and A are constants respecting different values for rod-type and conductor-type gaps and R is a function of electrode configuration and the gap distance d . Besides the continuous leader inception voltage V_{lc} the

leader voltage drop ΔV_l has to be expressed. Rizk formula for leader voltage drop is based on the assumption that the leader conductance per unit length G is given by Hochrainer's dynamic equation, which for the constant current leader propagation has a form:

$$G(t) = G_\infty + (G_i - G_\infty)e^{-\frac{t}{\theta}}, \quad (4.9)$$

where t is the lifetime of the leader section, G_i and G_∞ are the initial and ultimate values and θ is a time constant.

Assuming the constant speed of leader propagation and the leader gradient E_l is related to the conductance per unit length G and the leader current I_l by

$$E_l = \frac{I_l}{G}, \quad (4.10)$$

the proposed final formula for the leader voltage drop can be written as:

$$\Delta V_l = l_z E_\infty + x_0 E_\infty \ln \left(\frac{E_i}{E_\infty} - \frac{E_i - E_\infty}{E_\infty} e^{-\frac{l_z}{x_0}} \right), \quad (4.11)$$

where E_i and E_∞ are the initial and ultimate leader gradient, l_z is the axial leader length and $x_0 = v_l \theta$.

The final stage of the leader propagation the "final jump" occurs when the streamer zone reach the opposite electrode. As the streamer zone becomes shorter, its average field increases. It leads to the higher leader velocity as high as 10^9 cm/s at $E \approx 20$ kV/cm [44].

Chapter 5

Experimental flashover performance investigation of polluted and ice covered insulators exposed to impulse voltages

Most of the studies related to this topic are so far focused on AC or DC voltages, and only a small part is dedicated to transient overvoltages [45–47]. Moreover, these studies usually make use of empirical models which cannot capture the factors connected with material behavior and fundamental physics of discharges. The experimental investigation of flashover voltage under the ice condition was performed with an ice model in [48], for the post station insulator in [49]. The numerical model for a semiconducting glazed standard post insulator based on the FEM method was presented in [50]. The results of these investigations showed that ice has an influence on the flashover performance in the case of lightning or switching impulses. Reduction in flashover voltage is more evident for switching than lightning impulses (21 % reduction for positive polarity and 36 % for negative polarity [49]). The polarity effect of breakdown voltage, in case of wet ice condition, is that flashover voltage is lower for a positive than a negative polarity. For a dry ice surface, however, flashover voltage is lower for a negative polarity [48]. Results from the experiments with post station insulators show that flashover voltage is lower for a positive polarity for both dry and wet ice conditions [49]. The experimental measurements performed were focused on flashover performance investigations of polluted or ice-covered line insulators under transient overvoltage conditions. The behavior of insulators under the

slow and fast transients is usually demonstrated by lightning and switching impulse tests. In this study, the flashover characteristics of dry insulators and insulators artificially covered by pollution and ice will be determined when they are exposed to switching and lightning impulses of both polarities. In addition, the dependency of flashover voltage on the various front time of impulses will be investigated to confirm preliminary observations that the fast transients have no significant influence on the flashover voltage. The determination of the maximal equivalent frequency of impulses at which the difference of V_{50} between dry and ice conditions is minimal can be interesting and useful for insulation system producers and designers. Comparison of volt to time lag characteristics of insulator strings, an important feature for insulation coordination in electrical power systems, was also experimentally determined and evaluated.

5.1 Experimental setup

Experimental measurements were carried out in the setup according to Fig. 5.1. The impulse voltage generator (HighVolt IP 40/800L) consists of eight stages and the theoretically reachable peak voltage maximum is 800 kV at 40 kJ of energy. The impulse generator is fully controlled by SGB 1 operator device. The output voltage is measured by damped capacitive impulse voltage divider when its total capacity together with the capacity of high voltage bushing and capacity of a test object creates the load capacity of the impulse generator. The leakage current can be measured by coaxial shunt R_s with the resistivity of 200 $m\Omega$ and connected directly to the ground branch of the circuit. The coaxial shunt is frequency independent up to 1 MHz. The voltage and current waveforms are recorded by 8-bit digital scope with maximal sample rate 1 GSa/s.

The insulator was placed in a vertical climatic room at CIGEL laboratory with dimensions 6 x 6 x 9 m (w x l x h). The climatic room is equipped by spraying system which consists of eight pneumatic nozzles and fans with variable speed control. The temperature inside the chamber can be controlled up to the maximal value of $-60\text{ }^\circ\text{C}$. The output voltage from the impulse generator is led to the climatic room through high voltage bushing. The tested suspension glass insulator string consists of six standard profile insulators of 280 mm in diameter, spacing 147 mm and creepage distance 380 mm, see Fig. 5.2. The end of the insulator string was equipped by the grading ring to homogenize nonuniform electric field.

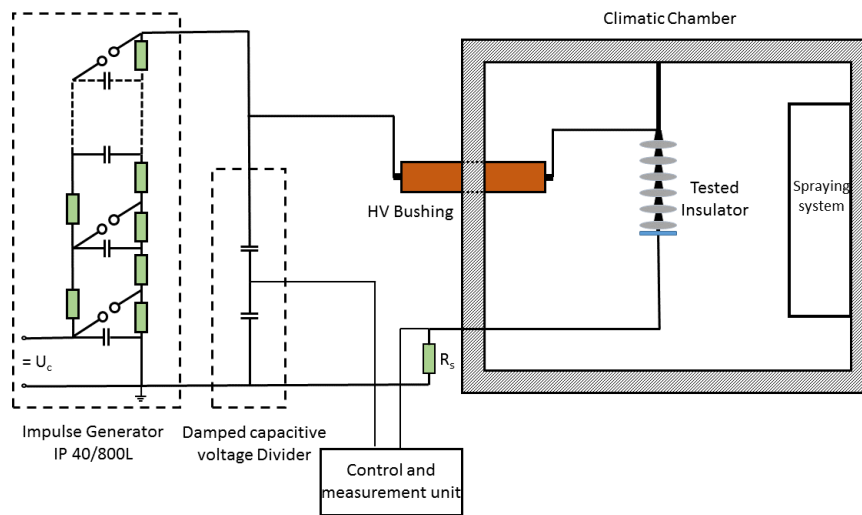


Figure 5.1: Test circuit for insulator in climatic chamber



Figure 5.2: Test circuit for insulator in climatic chamber

5.2 Ice formation and test procedure

The ice on insulator surface was created from supercooled droplets produced by spraying system that sprays into a uniform airflow obtained from the system of fans. Water conductivity of $80 \mu S/cm$ were prepared by addition of sodium chloride NaCl to de-ionized water. The water conductivity was kept constant during all the tests and was verified at the beginning of each test procedure. The insulator was energized by ac operating voltage during the ice accumulation phase. The ice quantity was determined by measuring the ice thickness increment on monitoring cylinder placed at the place of tested insulator, see Fig. 5.3. The increment of ice thickness with time is shown on Fig. 5.4.



Figure 5.3: Monitoring cylinder

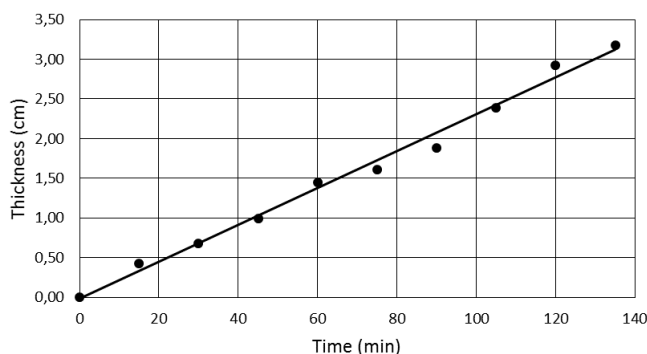


Figure 5.4: Time dependency of ice thickness on monitoring cylinder

The flashover test was performed according to melting regime test procedure standardized in [51]. This procedure consists of three consecutive stages. In the first stage, the ice is created at temperature $-12^{\circ}C$ for an appropriate time which is given for required thickness by the graph in Fig.5.4. After that, the 15 min ice hardening period is performed. During this period, the ac source is reconnected to the impulse generator. Then the temperature is increased above $0^{\circ}C$ to start the melting process. This stage is confirmed visually as the water film was present at the ice surface. The last stage was the impulse voltage test when the standard up and down method was used to determine flashover voltage V_{50} and standard deviation s . The maximum

likelihood method for normal distribution was used for the parameters evaluation of this voltage test.

The three shapes of impulses were generated to investigate the flashover performance of insulator covered by an ice layer:

- Lightning impulse (LI) with front time $1.2 \mu s$ and half time $50 \mu s$
- Switching impulse (SW-1) with front time $100 \mu s$ and half time $2500 \mu s$
- Switching impulse (SW-2) with front time $250 \mu s$ and half time $2500 \mu s$

These impulses represent different frequency content and transients in electrical power systems. Determined characteristics and results are presented in next section.

The example of iced insulator after the ice creation stage is shown in Fig. 5.5. The path of the arc during the impulse high voltage test can be traced on Fig. 5.5.



Figure 5.5: Tested insulator string after the ice accumulation stage (left), the arc trajectory (middle) and the detail of the arc trajectory for two bottom insulators (right)

5.3 Experimental results

5.3.1 Influence of ice thickness on insulator flashover voltage

The flashover voltage for impulse voltages and ice layer thickness in the range up to approximately 3 cm are shown in Fig. 5.6, Fig. 5.7 and Fig. 5.8. The

errors bars represents the determined standard deviation of flashover voltage extended by coefficient $k=2$ to reach 98 % probability. This error doesn't exceed the value of 16 kV for all measured values.

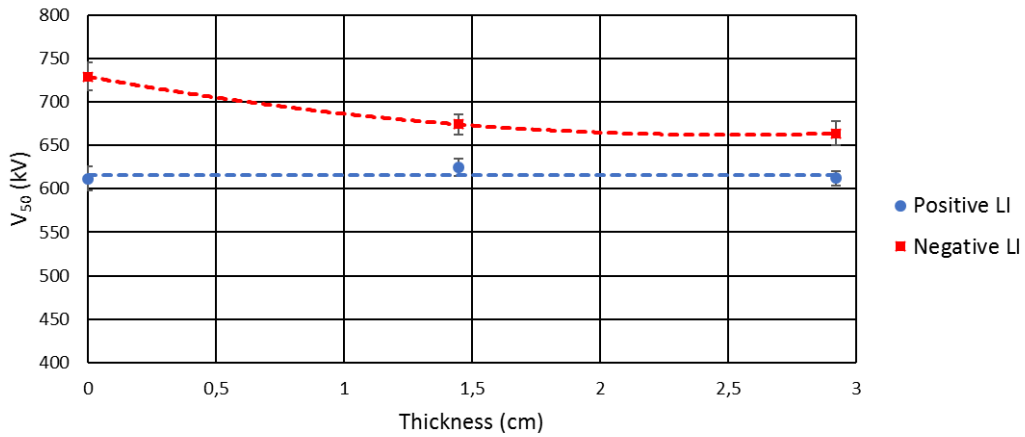


Figure 5.6: Flashover voltage V_{50} for lightning impulse (1.2/50 μs) of both polarities as ice layer thickness dependency

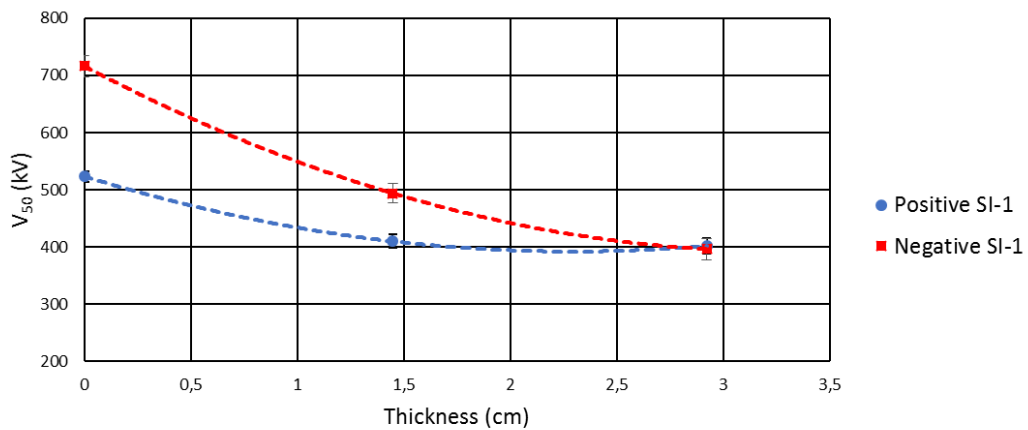


Figure 5.7: Flashover voltage V_{50} for switching impulse (100/2500 μs) of both polarities as ice layer thickness dependency

As can be seen from determined flashover voltages for the clean insulator the values have decreasing tendency with increasing front duration of the impulse. This effect was described by many tests in the past for various arrangements [1] and it may be considered as a proof of results validity. In case of lightning impulses, see Fig. 5.6 is the influence of ice layer on

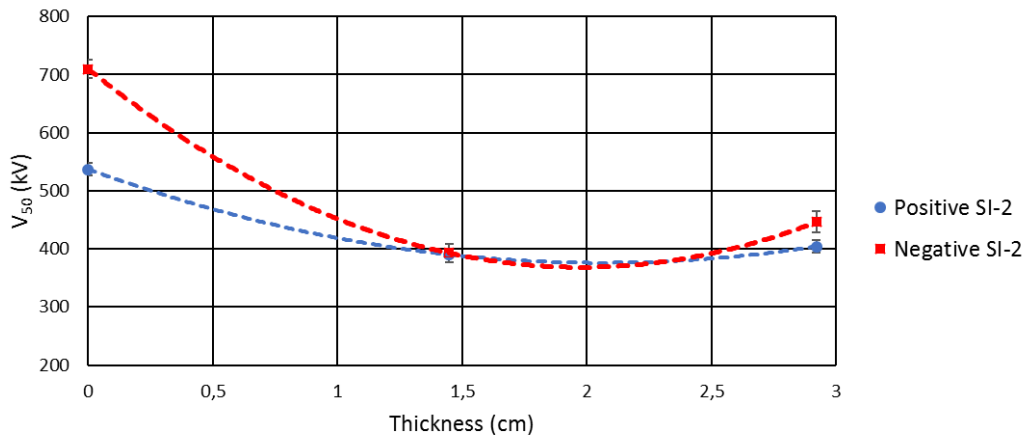


Figure 5.8: Flashover voltage V_{50} for switching impulse ($250/2500 \mu s$) of both polarities as ice layer thickness dependency

flashover voltage very small. The flashover voltage is significantly reduced only for negative polarity, approximately 8 %. On the other hand for the investigated switching impulses, see the Fig. 5.7 and Fig. 5.8, the flashover voltage reduction reached the value of 25 % for positive polarity and 44 % for negative polarity.

The influence of ice layer thickness on flashover voltage is evident from Fig. 5.7 and Fig. 5.8. For the switching impulse SI-1, characterized by faster front duration, the flashover voltage has still decreasing tendency in the ice layer thickness up to 3 cm. However, for the switching impulse SI-2 with longer front duration there is a significant increase of the flashover voltage for the higher thickness of ice layer, and the determined curves have a minimum value.

5.3.2 Voltage-time characteristic

The voltage-time characteristic for lightning and switching impulses for the clear insulator, insulator covered by ice layer of 1.45 cm and 2.92 cm in thickness are shown in Fig. 5.9, Fig. 5.10, Fig. 5.11, Fig. 5.12, Fig. 5.13 and Fig. 5.14. Due to the larger scatter of results, mainly in the cases when the ice layer was applied, the results were processed by using statistical methods. Nevertheless, especially for the lower voltages where the breakdown probability is very low, the statistical approach was not possible.

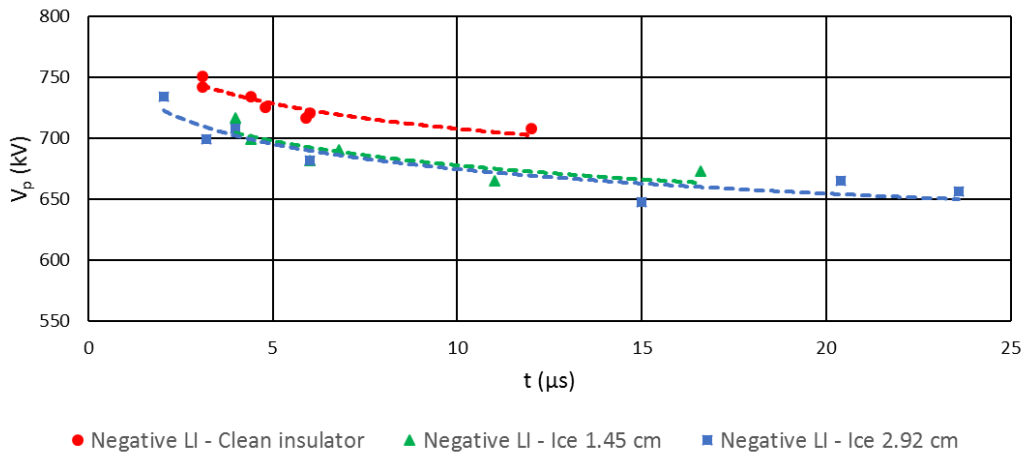


Figure 5.9: Voltage - time characteristic for negative lightning impulse (1.2/50 μs) and two ice layer thicknesses

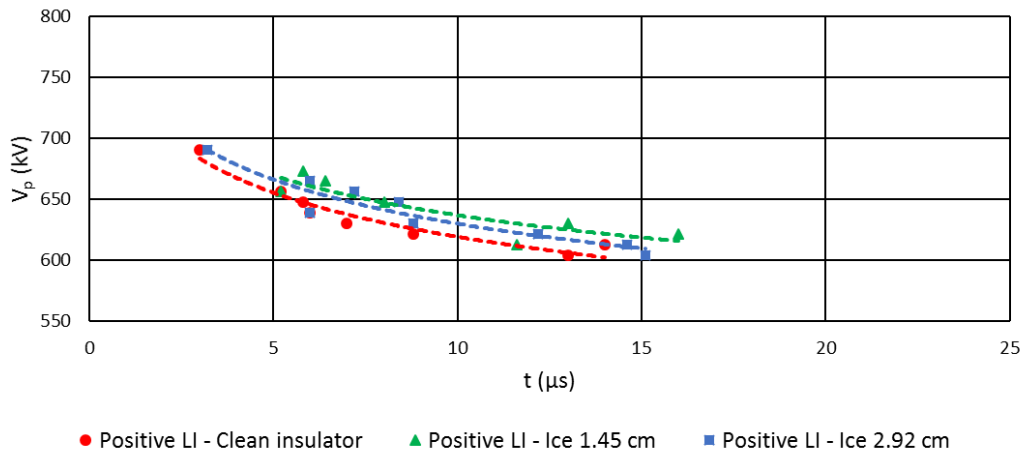


Figure 5.10: Voltage - time characteristic for positive lightning impulse (1.2/50 μs) and two ice layer thicknesses

Determined volt-time characteristics correspond to the flashover voltages presented in the previous section. There is a significant reduction of the flashover voltage when the ice layer is present. Further, the breakdowns have a tendency occur in longer time at voltages close to the lower boundary of uncertainty zone than in the case without an ice layer.

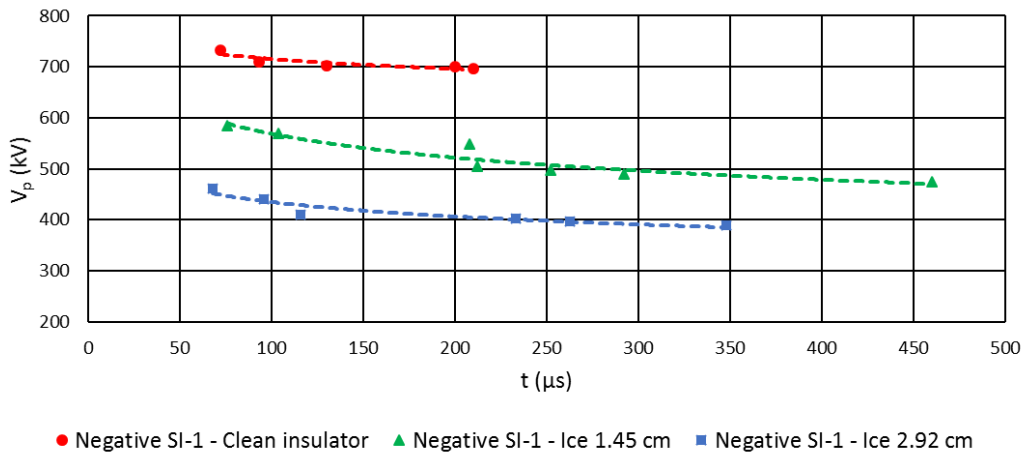


Figure 5.11: Voltage - time characteristic for negative switching impulse (100/2500 μs) and two ice layer thicknesses

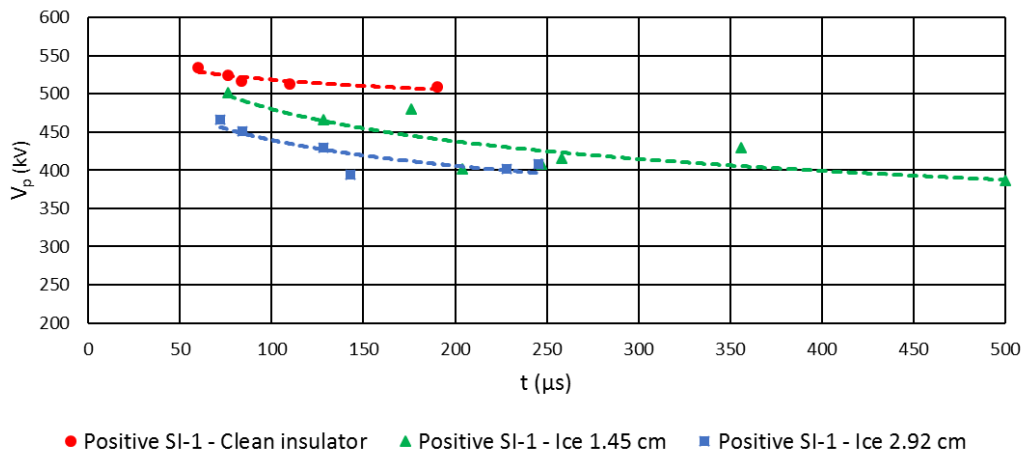


Figure 5.12: Voltage - time characteristic for positive switching impulse (100/2500 μs) and two ice layer thicknesses

5.4 Arc propagation along an ice covered insulator

The development and propagation of arc in case of impulse voltages is very fast in compare to the ac or dc voltages. Therefore, the using of a high speed camera with higher frame per second (fps) rate is required. Assuming the mean value of leader advancement velocity in the range of $2 \cdot 10^4$ m/s the camera speed should be higher than 50 000 fps. However, the maximally

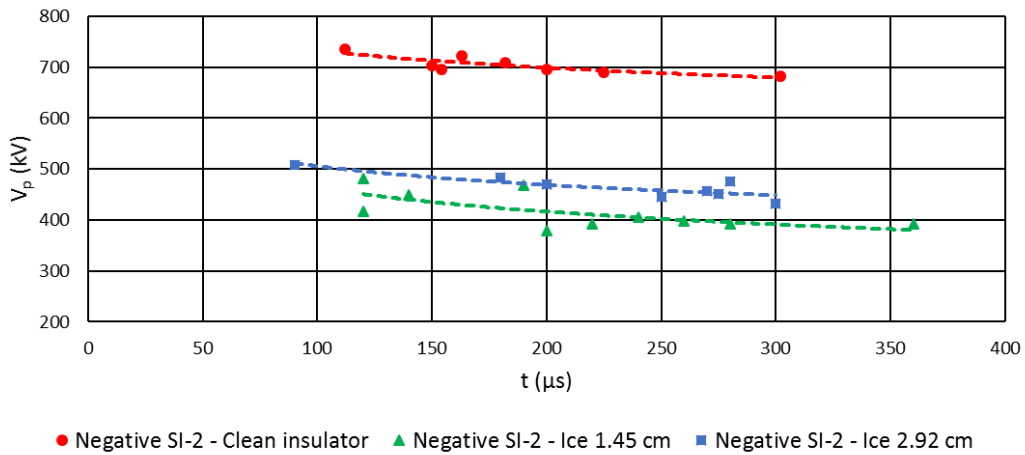


Figure 5.13: Voltage - time characteristic for negative switching impulse (250/2500 μs) and two ice layer thicknesses

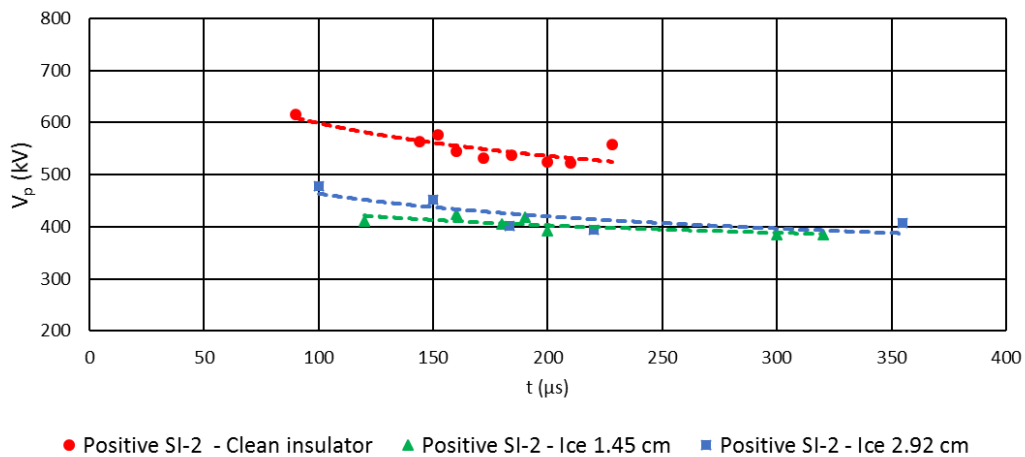


Figure 5.14: Voltage - time characteristic for positive switching impulse (250/2500 μs) and two ice layer thicknesses

provided frame resolution is then reduced to 512 x 128, pixels and it is not easy to record the arc development along the all insulator string in sufficient detail. Moreover, the insulator string has a diverse structure, and the arc can be partly hidden behind. Finally, there is an unpredictable behavior of the arc. All the mentioned issues make the recording of the arc propagation very demanding discipline, especially in the case of real insulators.

Some interesting pictures captured by Photron Fastcam SA 1.1 high speed camera are presented in following figures. In Fig. 5.15 is a detail of the arc

trajectory between two caps of string insulator recorded with 75 000 fps. The applied impulse voltage is 450 kV 250/2500 μs and the surface was covered by ice layer of 1.45 cm in thickness. The first two frames show the path of the leader which copying the surface of the insulator. The fourth and fifth frame show the situation after the arc initiation.



Figure 5.15: Arc trajectory between two insulators (recorded by high speed camera 75 000 fps)

The Fig. 5.16 shows the same situation when the voltage was applied few minutes later after the previous test. As can be seen, the trajectory is quite different from the first record. The arc is bridging the caps at this time not copying the insulator surface.

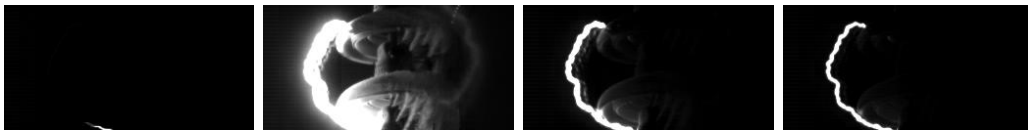


Figure 5.16: Arc trajectory between two insulators (recorded by high speed camera 75 000 fps)



Figure 5.17: Arc trajectory along the insulator string (recorded by high speed camera 10 000 fps)

The arc trajectory along the insulator string can be seen from Fig. 5.17. The applied impulse voltage was 560 kV 250/2500 μs and the surface was covered by ice layer of 1.45 cm in thickness. The speed of the camera has to be decreased to 10 000 fps to get reasonable frame resolution and thus it

was not possible to record the leader before the arc initiation. However, from the recorded arc path is clear how the leader propagates along the ice surface.

Chapter 6

Mathematical simulation of flashover process

6.1 Obenaus basic concept

Obenaus in 1958 was probably the first who proposed a quantitative model for flashover phenomena on the surfaces covered by a conductive layer. He substituted the whole process by an electrical circuit constituted of an arc in series with resistance R_p , see Fig. 6.1.

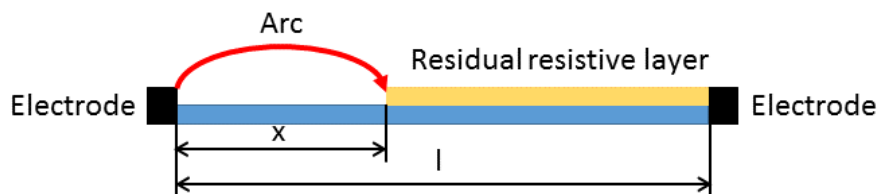


Figure 6.1: Obenaus model

The applied voltage is the addition of arc and residual resistive layer voltage drops. The concept itself is simple and general, but it is necessary to obtain an appropriate equation for the arc voltage drop and resistance of residual layer supported by physical theory. The flashover models very often include parts which are based on experimental observations since the theory is too complicated or not available at all.

6.1.1 Arc models

Until now, many arc models have been developed. However, just a few of them are used more frequently by engineers. The fundamental one is undoubtedly the Ayerton's arc model which is based on an approximation of experimental measurements. The voltage gradient E_{arc} can be approximated by following equation:

$$E_{arc} = AI_{arc}^{-n}, \quad (6.1)$$

where I_{arc} is the arc current, and A and n are constants. The constant values for various conditions are summed in Tab. 6.1 [52]. As can be seen from the table, the constant A has a range from 30 to 310 and constant n from 0.1 to 1.38. The high variation is due to their dependency on the ambient atmospheric conditions, the medium in which the arc propagates, the voltage waveform, the surface of an insulation layer. All these factors can influence the arc propagation and its behavior.

Another group of models describe the arc by the combination of fluid dynamics, thermodynamics and Maxwell's equations. However, the theoretical description of arc plasma is extremely complex in detail so that the complete mathematical models are not possible, and some simplification has to be always involved. Generally, the conductance of an arc channel varies with supplied power and transported power. The power accumulated in arc channel Q can be expressed as:

$$Q = \int_0^t (P_{in} - P_{out})dt \quad (6.2)$$

and the instantaneous arc conductance g can be defined as

$$g = F(Q) = F\left(\int_0^t (P_{in} - P_{out})dt\right). \quad (6.3)$$

The change of conductance divided by instantaneous conductance is then

$$\frac{1}{g} \frac{dg}{dt} = \frac{1}{g} \frac{dF(Q)}{dQ} \frac{dQ}{dt}. \quad (6.4)$$

Finally, the general arc equation has a form of

$$\frac{d(\ln g)}{dt} = \frac{F'(Q)}{F(Q)} (P_{in} - P_{out}). \quad (6.5)$$

Cassie and Mayer introduced simplified models for qualitative simulations of arc phenomena. The arc is considered as plasma in local thermodynamic

Investigator	Current(A)	A	n	Excitation	Medium
SuitsandHocker(1939)	1-10	65	0.6	NS	air
		220	0.6	NS	stem
		81	0.6	NS	nitrogen
Obenause et al.(1958)	0.1-15	63	0.7	ac	air
L.Alstonetal et al.(1963)	0.1-2	100	0.76	ac	air
E.Nasseretal et.al.(1963)	0.1-1	63	0.76	dc	air
Hampton(1964)	0.1-0.5	65	0.8	NS	air
		52	0.1	NS	steam
E.Lose et al.(1971)	1-3	52	0.43	dc	air
	NS	44	0.67	dc	air
Nottingham(1973)		310	0.985		
		39.2	0.67		
		203	1.38		
Claverie et al.(1973)	1-2	113	0.5	ac	air
		98.99	0.5		
Jollye et al.(1974)	1-3	296	0.397	ac	air
El-Arbatye et al.(1979)	NS	40	0.8	ac	air
F.A.M.Rizk(1981)	0.05-2.0	130	0.45	dc	air
		210.6	1.3		
Gers et al.(1981)	0.1-5	46.05	0.91	dc	air
		44.77	0.822	impulse	
		43.80	0.822	dc	
		59.64	0.773	dc	
M.P.Verma(1983)	NS	53.45	0.5	ac	air
	NS	40.6	0.724	dc	air
Mayr et al.(1986)		50.20	0.708		helium
		114	0.714		nitrogen
D.A.Swift(1989)	1-3	80	0.5	dc	air
		60			
G.Zhicheng et al.(1990)	0.1-1.0	138	0.69	dc	air
		140	0.67	ac	
F.L.Topalis(1992)	NS	131.5	0.374	NS	air
R.Sundararajan et al.(1993)	NS	60	0.8	dc	air
		63	0.5		
R.P.Singh et al.(1994)	NS	31	0.43	ac	air
		100	0.98		
N.Chatterjee et al.(1995)	NS	NS	0.7	ac	air
H.G.Gopal et al.(1995)	NS	60	0.25	NS	air
		100	1.20		
D.C.Chaurasia et al.(1996)	0.01-1.2	50	0.25	ac	air
		100	1.1		
A.S.Farag et al.(1997)	NS	30	0.24	ac	air
M.Farzaneh et al.(2000)	NS	84	0.77	dc-	air on the ice
		209	0.45	dc+	
		205	0.56	ac	
J.P.Holtzhausen(2001)	NS	59	0.53	ac	air

Table 6.1: Constants of Ayerton's model for various conditions

equilibrium. The Cassie model assumes that the arc channel has the shape of a cylinder which is filled by highly ionized gas at constant temperature. The constant current density is assumed it means that the cross section area is changing with current. Other assumptions are the constant resistivity and heat content per unit. Than,

$$g = F(Q) = dg_0 = \frac{Q}{Q_0} g_0 \text{ and } F'(Q) = \frac{g_0}{Q_0}, \quad (6.6)$$

$$Q = dQ_0 \text{ and } P_{out} = dP_0 = Q \frac{P_0}{Q_0}. \quad (6.7)$$

Substituting the assumption (6.6) and (6.7) into the general arc equation (6.5)

$$\frac{d(\ln g)}{dt} = \frac{P_0}{Q_0} \left[\left(\frac{u_a}{u_0} \right)^2 - 1 \right], \quad (6.8)$$

where $u_0 = \sqrt{\frac{P_0}{g_0}}$ is the static voltage and u_a is the arc voltage.

Mayer assumed the arc cylinder with a constant diameter which means that the conductivity strongly depends on temperature (exponentially) and is independent of the cross-sectional area. Mayer further assumed that the relation between voltage and current is constant, so the cooling of arc channel is constant as well. If we take into the consideration the assumption

$$g = F(Q) = ke^{\left(\frac{Q}{Q_0}\right)} \text{ and } F'(Q) = \frac{k}{Q_0} e^{\left(\frac{Q}{Q_0}\right)}, \quad (6.9)$$

the Mayr arc equation has a form of

$$\frac{d(\ln g)}{dt} = \frac{1}{Q_0} (u_a i_a - P_0). \quad (6.10)$$

The Mayr equation is representative for small currents close to the zero when the arc temperature doesn't exceed 8000 K. Otherwise, the Cassie equation is valid for high currents above the temperature of 8000 K. Many models combining the Cassie and Mayr equations have been proposed to simulate arc behavior in the electrical power engineering, e.g. [53–55].

6.1.2 Resistance of the conductive layer

The pollution layer created on insulator during the line operation may caused an increase of surface conductivity. The resistance element of pollution layer is

$$dR = \frac{dl}{\gamma(l)2\pi r(l)}, \quad (6.11)$$

where l is the shortest path between electrodes along the insulator surface, $\gamma(l)$ is the surface conductivity and $r(l)$ is the radius of the surface at element dl .

The total resistance of pollution layer between two electrodes is

$$R = \int_0^L \frac{dl}{\gamma(l)2\pi r(l)}, \quad (6.12)$$

where L is the total length of leakage path. Assuming that γ_m is the mean conductivity of pollution layer the equation (6.12) can be expressed as

$$R = \frac{1}{\gamma_m} \int_0^L \frac{dl}{2\pi r(l)} = \frac{f}{\gamma_m}, \quad (6.13)$$

where f is known as form factor which is the characteristic parameter of insulators. This concept of resistance calculation was used by Bohme and Obenaus in their original model [56].

Woodson and McElroy introduced a simplified model as a surface with circular geometry and constant surface resistivity [57]. The geometry is shown in Fig. 6.2.

The resistivity of wet polluted layer of a disk insulator was determined as

$$R = \frac{B(r, R_a, R_0)}{\gamma_m}, \quad (6.14)$$

where B is the dimensionless geometric factor depending on the radius r of the outer extremity of the discharge, the radius R_a of the discharge root in the wet contaminant, and the radius R_0 of the outer electrode. It was found that B can be assumed independent of R_a where the error does not exceed 30 % [57]. The parameter B may be determined as a function of $R_0 - r_{max}$ where the r_{max} is the maximal radius to which a discharge can grow with an applied voltage. The experimentally determined function $B(r_{max}, R_0)$ is

$$B(r_{max}, R_0) = 1.610^{-2}(R_0 - r_{max})^{1.4}. \quad (6.15)$$

A model for the case of a discharge burning on a polluted rectangular strip is introduced in [16] by Wilkins.

Assuming the discharge roots to be circular and rectangular strip, see Fig. 6.3 two cases of solution for resistance R were developed. For the

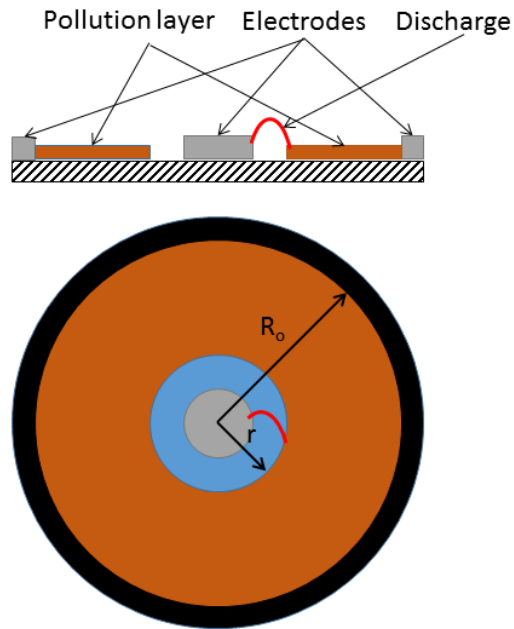


Figure 6.2: Woodson and McElroy idealized model

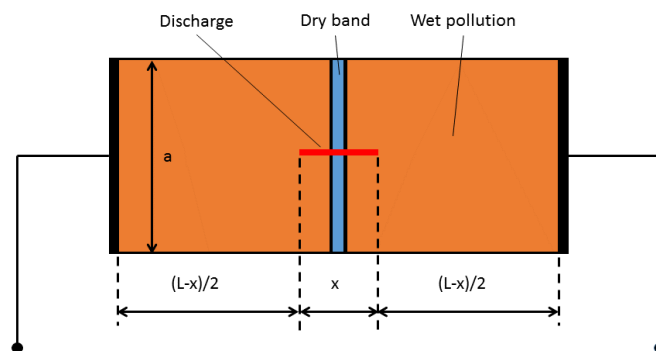


Figure 6.3: Wilkins model for flashover of a polluted strip

narrow strip, where the width of the series pollution layer is less than its length the resistance is given by

$$R = \frac{1}{2\pi\gamma_m} \left(\frac{\pi(L-x)}{a} + \log \left(\frac{a}{2\pi r_d} \right) \right), \quad (6.16)$$

where r_d is the radius of the discharge root. For the wide strip, where the width of the series pollution layer is greater than about three times its length the resistance is given by

$$R = \frac{1}{2\pi\gamma_m} \left(\log \left(\frac{2L}{\pi r_d} \right) + \log \tan \left(\frac{\pi x}{2L} \right) \right). \quad (6.17)$$

The radius r_d of the discharge root is a function of current i

$$\frac{i}{\pi r_d^2} = \text{const.} \quad (6.18)$$

Either expression 6.17 or 6.18 may be used with reasonable accuracy if the width and length of the strip are of the same order.

6.2 Dynamic numerical model of discharge propagation on insulator string

The numerical model is based on the physical streamer-leader process in long air gaps presented by many authors in various modifications. A complete mathematical description of this physical process is very difficult and some parts even still remain unclear. This is the reason why researchers usually work with simplified mathematical equations to find optimal model regarding purposes of simulations. Generally, the more often used streamer-leader models are coupled with a calculation of the electric field distribution and streamer and leader propagation. The electric field distribution can be in some cases (e.g. rod-plate gaps) expressed by analytical formulas, however nowadays are more frequent are the numerical calculations using FEM. The streamer and leader initiation and propagation model is usually partly based on experimentally determined characteristics and parameters. The physical background of the streamer-leader flashover process with assumptions and constrains for mathematical simulations was described in detail in chapter 4. The following describe the simulation model for prediction of flashover voltage of suspension insulator during the impulse high voltage testing under the pollution and ice condition. Proposed model was built up for the purposes of validation of experimental results and also as a tool for the flashover voltage prediction.

corona zone is a function of the area between the potential distributions before and after streamer formation, see Fig. 6.5.

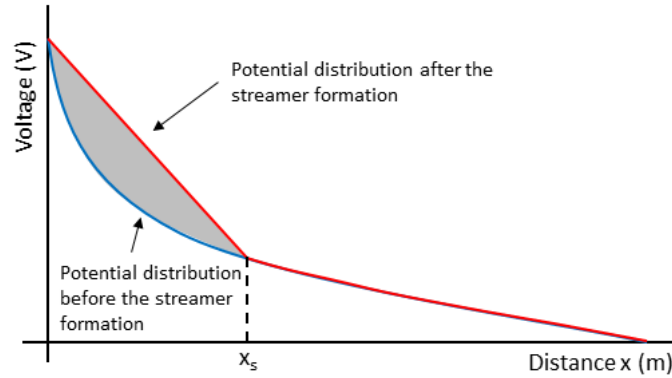


Figure 6.5: Potential distribution before and after the streamer formation

It is assumed, that the stable propagating leader is initiated when the critical total charge increment $\Delta Q_c = 1 \mu C$ is reached. The total charge increment is calculated according to equation (4.5). The leader extension Δx_L is then calculated from the leader velocity, see equation (4.7). The constant q_l is assumed as average value $45 \mu C/m$ and the charge of the streamer zone in front of the leader's head ΔQ is calculated from equation (4.5). The streamer-leader system step by step propagates along the insulator and in the moment when across the whole distance L the flashover occurs. If during the process the charge increment is less than zero the whole process is stopped, and no flashover occurs.

6.2.2 Electric field calculation

The electric field distribution has a crucial role in the discharge propagation process. The electric field distribution is rapidly changing in time when the impulse voltage is applied. Analytical solutions are possible only for simple electrode cases and the more precise numerical calculations like FEM have to be involved. However, FEM requires the exact geometrical description of insulator arrangement and a large amount of computation time. On the other hand, the proposed simulation model needs relatively fast recalculation of the electric field during the simulation process. The simple and enough accurate solution could be the representation of the insulation string as an equivalent circuit with distributed parameters while parameters of passive elements are adjusted to approximate the voltage distribution $V(x)$ determined from FEM calculation at the time when the impulse reach the maximum voltage. Then,

the voltage distribution function $V(t, x)$ can be derived from the equivalent circuit equations.

The equivalent circuit of insulator string is shown in Fig. 6.6.

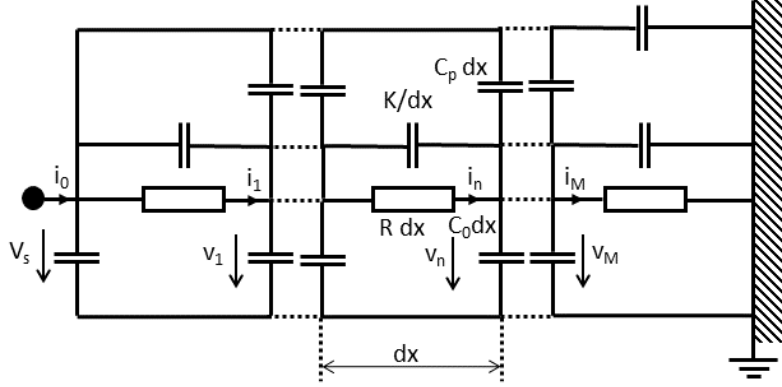


Figure 6.6: Equivalent circuit of insulator string

The circuit consists of resistor R (Ω/m), insulator to ground capacity C_0 (F/m), insulator to wire capacity C_p (F/m) and capacity of insulator K (Fm). In fact, these parameters are not constant with x coordinate and the linear or exponential function can be used to express this dependency. Sometimes the constant values are assumed to simplify calculations. From the voltage and current relations in an element dx and after some mathematical modifications the final partial differential equation has a form of:

$$\frac{\partial^4 v(t, x)}{\partial x^2 \partial t^2} + \frac{1}{RK} \frac{\partial^3 v(t, x)}{\partial x^2 \partial t} + \frac{C_p}{K} \frac{\partial^2 (v(t, x) - V_s(t))}{\partial t^2} - \frac{C_0}{K} \frac{\partial^2 v(t, x)}{\partial t^2} = 0, \quad (6.19)$$

where $v(t, x)$ is the instantaneous voltage at time t and distance x from high voltage electrode and $V_s(t)$ instantaneous voltage of the source. Impulse voltage $V_s(t)$ can be described by double exponential model. The equation (6.20) can be solved by numerical methods only. Assuming the continuous time and discrete distance x we can make a decomposition into the system of differential equations of first order. Each n -th element is then described by pair of equations:

$$K \left(\frac{d(v_{n-1}(t) - v_n(t))}{dt} - \frac{d(v_n(t) - v_{n+1}(t))}{dt} \right) + i_n(t) - i_{n+1}(t) + C_p \frac{d(V_s(t) - v_n(t))}{dt} - C_0 \frac{dv_n(t)}{dt} = 0,$$

$$v_{n-1}(t) - v_n(t) - Ri_n(t) = 0. \quad (6.20)$$

Thus, for n elements we get $2n$ equations with the same number of unknown currents and voltages. The resulted voltages and currents in each node are functions of time. The parameters R , K , C_p and C_0 are given by geometrical configuration, insulation material and also by pollution or ice layer on insulator surface.

The electrostatic field distribution of suspension glass insulator can be calculated in FEM software to get voltage distribution and approximations of equivalent circuit parameters. It is supposed rotationally symmetrical geometry of insulator thus the 2D model can be built up. Respecting experimental measurements described in chapter 4 the high potential is placed on the top of the insulator string, and the ground is connected to the shielding ring placed at the end of insulator string. The voltage distribution is then in opposite direction than in the case of a real insulator on a tower of overhead line. The rest of the metallic parts has a floating potential. The polluted ice layer can be simulated as a parallel layer copying the insulator surface with given specific conductivity. As can be seen from experimental measurements in the cold room the ice layer and icicles morphology on insulator string may be varied. However for the higher thicknesses of ice (more than 1.5 cm) the particular insulators are almost fully bridged by icicles. The main assumption for the FEM geometry of insulator string covered by ice layer is that the ice layer bridges all insulator caps by a consistent layer of ice with appropriate thickness. The relative permittivity of the ice layer under switching impulse can be considered equal to the steady state permittivity 76. For the lightning impulse, the relative permittivity decreases to value between 3 and 4 [49]. The determined electric field distribution of insulator string consisting of six insulators is shown in Fig. 6.7 for dry condition and in Fig. 6.8 for polluted ice layer of 3 cm thickness.

The voltage distribution along the length of the insulator string for maximal voltage is shown in Fig. 6.9 and Fig. 6.10. Cutting lines are in the center of insulator, in the half of insulator radius and the insulator radius.

As can be seen from presented figures, the potential distribution along the insulator string is close to the linear distribution. The reason is that there are not present any large grounded parts or conductor during the high voltage tests which increase the capacity to the ground or capacity to the conductor.

The voltage distribution approximation can be used for the simulation of the flashover process. The Fig. 6.11 shows voltage distributions which are derived from the Fig. 6.9 and Fig. 6.10 respecting the resistance of the

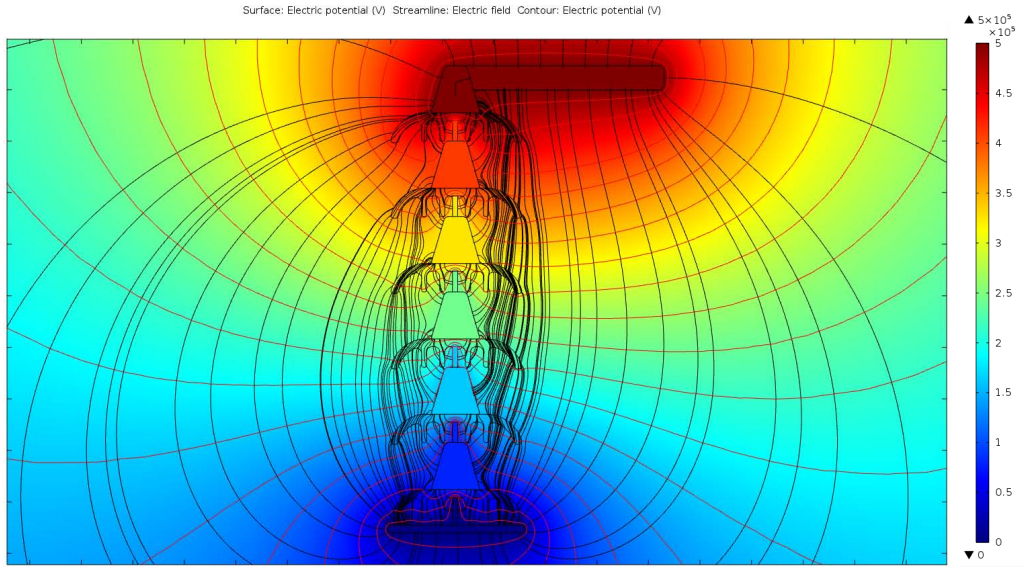


Figure 6.7: Electric field of suspension insulator string (applied voltage 500 kV)

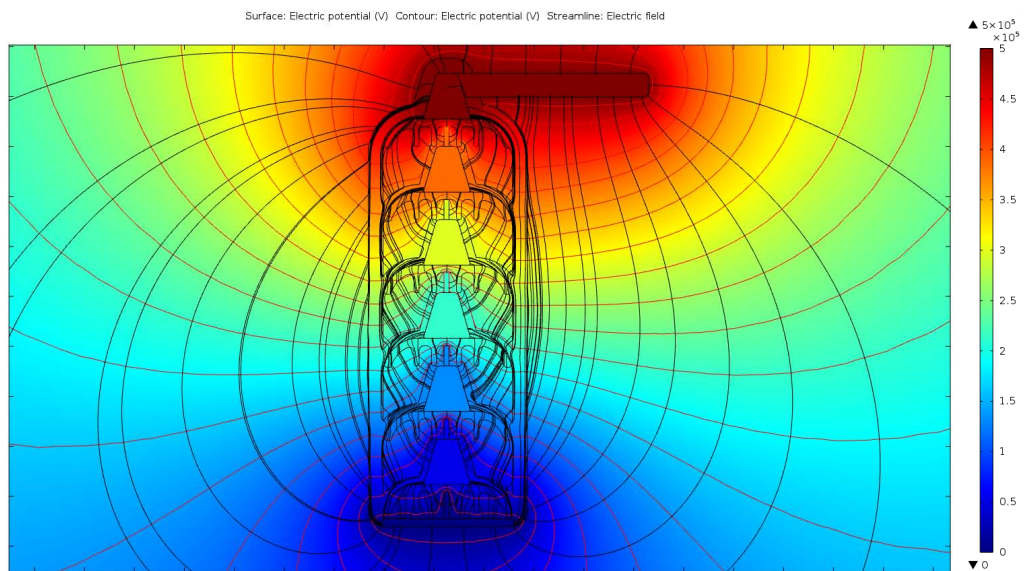


Figure 6.8: Electric field of suspension insulator string - 3 cm ice layer simulation (applied voltage 500 kV)

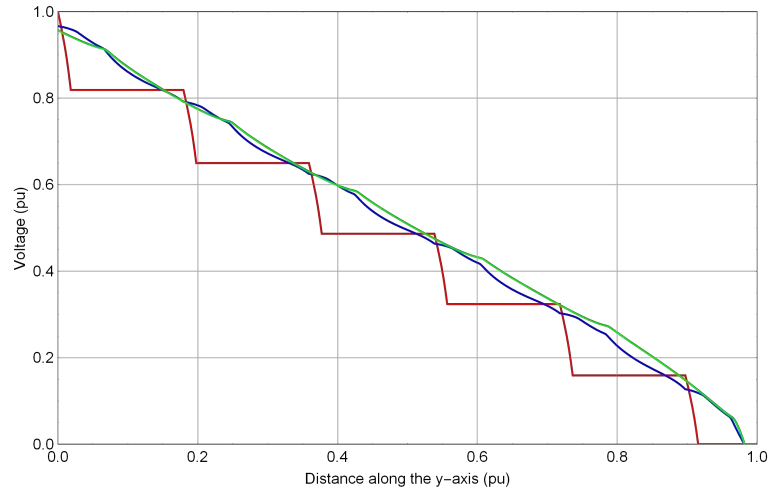


Figure 6.9: Voltage distribution along the length of the insulator string in the center (red), in the half radius of the insulator (blue) and in the maximal radius of the insulator (green)

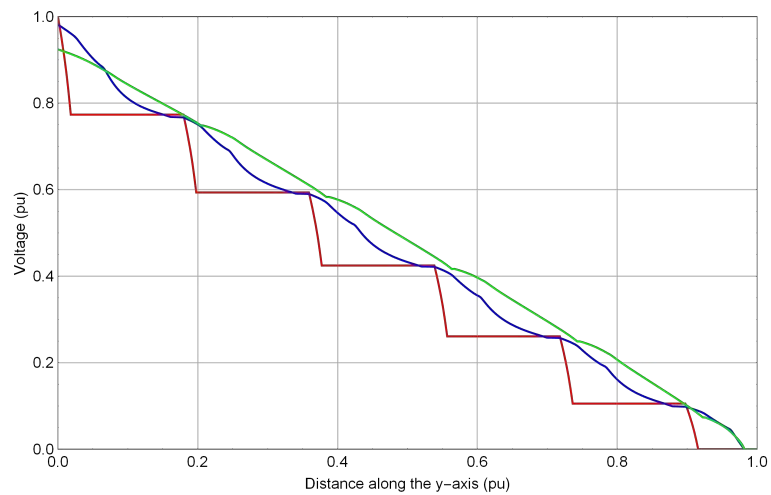


Figure 6.10: Voltage distribution along the length of the insulator string with 3 cm ice layer in the center (red), in the half radius of the insulator (blue) and in the maximal radius of the insulator (green)

polluted ice layer which can be estimated on the basis of various models described in chapter 6.1.2.

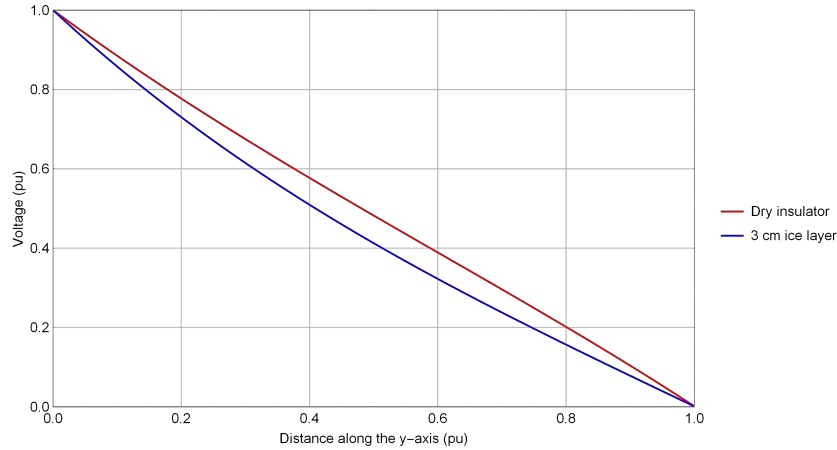


Figure 6.11: Approximation of voltage distribution along the length of the insulator string

6.2.3 Simulation results and verification

The above described mathematical model for flashover performance prediction of suspension insulator string was realized in Wolfram Mathematica[®]. Created mathematical model allow to calculate the streamer-leader propagation process for different shapes of impulse voltages of both polarities. This model can take into consideration an influence of pollution and icing condition. As the experimental measurement under the pollution and icing condition were performed the obtained results can be used for the verification of simulation model.

As the experimental measurements show, the switching impulses of positive polarity are more critical regarding flashover performance of suspension insulator under the polluted ice conditions. Thus, the simulation model was validated for such conditions and results were compared with determined data from laboratory experiments. The comparison of flashover voltage V_{50} for dry and two thicknesses of ice layer are shown in Fig. 6.12, comparison of voltage - time characteristic for dry insulator on Fig. 6.13 and the comparison of voltage - time characteristic for ice layer of 2.92 cm.

Presented results confirm that the proposed simulation model can give reasonable accurate values of flashover voltages which are sufficient for test

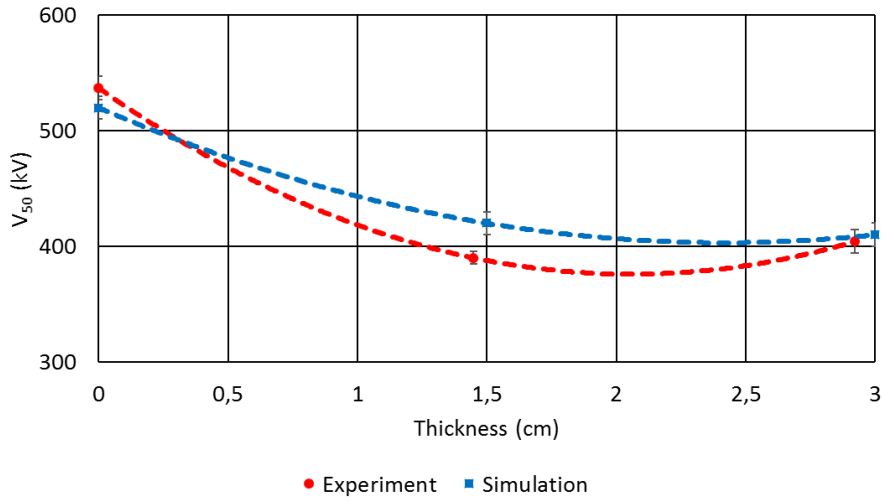


Figure 6.12: Flashover voltage V_{50} for switching impulse (250/2500 μs) as ice layer thickness dependency - comparison of calculated and experimental data

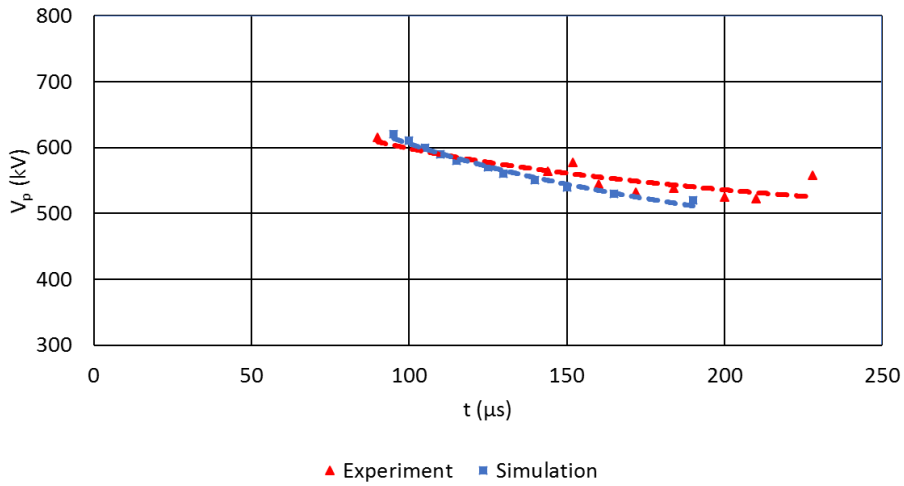


Figure 6.13: Voltage - time characteristic for switching impulse (250/2500 μs) fro dry insulator - comparison of calculated and experimental data

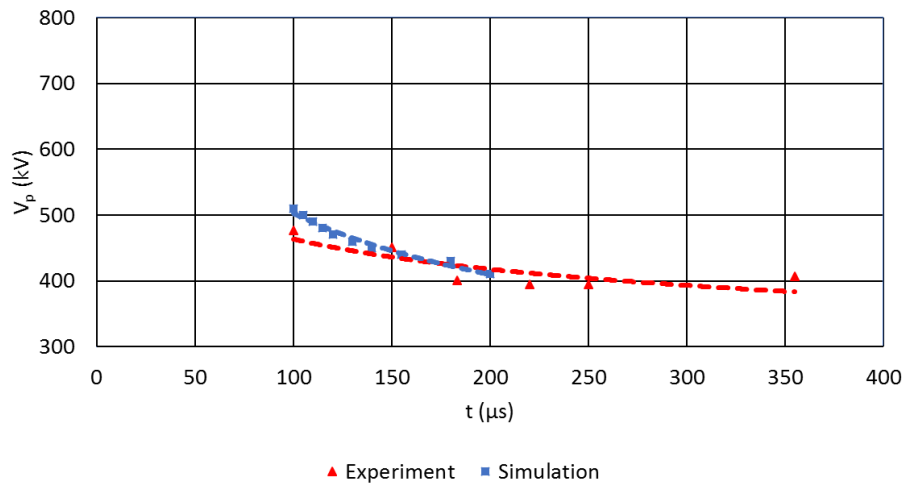


Figure 6.14: Voltage - time characteristic for switching impulse (250/2500 μs) for 2.92 cm ice layer - comparison of calculated and experimental data

engineers in high voltage laboratories and designers of insulation systems of overhead lines.

Chapter 7

Conclusion

The theses deal with some specific problems related to impulse high voltage tests. In chapter 2, are briefly presented standard high voltage test approaches and evaluation methods under dry, wet and cold conditions to introduce fundamental terminology and provide some background for following text.

Chapter 3 is dedicated to impulse voltage and current measurement. First, the methods for determining of frequency characteristic properties of voltage dividers are described and then applied to the standard voltage divider to show their unsuitability for fast-rise impulse measurements, how requires some IEC standards. The only possible solution is to complete the impulse voltage dividers from elements with very low parasitic inductance and capacitance. The research activities in this field are nowadays focused mainly on the using of ceramic disc resistors and liquid voltage dividers. The preliminary experiments with liquid high voltage resistors were performed, and 20 kV liquid impulse voltage divider was realized. The reached response time is roughly ten times better than in the case of common high voltage dividers. Thus, the liquid dividers seem to be promising alternatives of ceramic discs resistors. However, the long term stability and thermal stability of divider ratio must be further investigated to approve the application for high voltage laboratory purposes.

Further, the Rogowski coil as a sensor for impulse current measurement was introduced. The frequency dependency of Rogowski coil constant has to be known for purposes of current impulses measurement. The calibration circuit for wide frequency range was proposed, and two types of coil constructions were measured. After that, the influence of shielding was determined with the result that the reduction effect of resonant frequency of cross-wounded coil is not so significant in comparison with uniformly wounded coil. Finally,

the influence of Rogowski coil homogeneity and the shielding to the accuracy of measurement was shown.

The using of nanocrystalline alloys as a material of magnetic cores of instrument voltage and current transformers is discussed in the last part of this chapter. On the realization of impulse current transformer and voltage transformer is shown that the nanocrystalline magnetic core can be advantageously used as the magnetic circuit. On the other hand, the disadvantage of the nanocrystalline material is very high fragility and difficult machinability. The production of cut cores requires sophisticated approaches that always significantly reduce magnetic properties.

Chapter 4 is concerned with a physical background of streamer-leader propagation for a long air gap to provide a brief insight into the flashover processes in the air. This theory is further used in Chapter 5 and especially in Chapter 6.

Chapter 5 contains the laboratory study of flashover performance of polluted and ice covered suspension insulator exposed to impulse overvoltage. Experimental measurements were performed on a suspension string of cap and pin glass insulator in Industrial Research Chair on Atmospheric Icing of Power Network Equipment (CIGELE), University of Quebec at Chicoutimi. The effects of polluted ice layers on flashover performance and volt-time characteristics of insulators for lightning impulse and two switching impulses with different front time were investigated. Under icing and pollution conditions, when the insulator is covered with ice, it is found that in the case of lightning impulses flashover voltage is reduced only for negative polarity, by approximately 8 %. On the other hand for switching impulses, the flashover voltage reduction reached the value of 25 % for positive polarity, and 44 % for negative polarity. The flashover voltage reduction was almost the same for the switching impulse with 100 μs front time and switching impulse with 250 μs front time. Impulses with the front time slower than 100 μs did not reduce flashover voltage. The determined volt-time characteristics correspond to the flashover voltages when there is a significant reduction in flashover voltage when an ice layer is present.

The experimental results were further used for the validation of mathematical model simulating physical processes during flashover when various impulse voltages are applied. The algorithm of the simulation model is fully described in Chapter 6. The simulation model allow to calculate flashover voltages for different shapes of test impulse voltages and to take into consid-

eration an influence of pollution and icing condition. Presented comparison with experimental measurement confirms that the proposed simulation model can give reasonable accurate values of flashover voltages which are sufficient for test engineers.

Bibliography

- [1] J. Kuffel, E. Kuffel, and W.S. Zaengl. *High Voltage Engineering Fundamentals*. Elsevier Science, 2000.
- [2] *IEC 60060-1 High Voltage Test techniques. Part 1: General Definitions and Test Requirements*, IEC Standard, 1989.
- [3] T.R. McComb and J.E. Lagnese. Calculating the parameters of full lightning impulses using model-based curve fitting. *Power Delivery, IEEE Transactions on*, 6(4):1386–1394, Oct 1991.
- [4] J. Perez and J. Martinez. Digitally recorded lightning impulse with overshoot parameter evaluation by using the kalman filtering method. *Power Delivery, IEEE Transactions on*, 13(4):1005–1014, Oct 1998.
- [5] Y.M. Li, J. Kuffel, and W. Janischewskyj. Exponential fitting algorithms for digitally recorded hv impulse parameter evaluation. *Power Delivery, IEEE Transactions on*, 8(4):1727–1735, Oct 1993.
- [6] L. Angrisani and P. Daponte. A proposal for the automatic evaluation of the mean curve required by the ansi/ieee std 4-1978. *Instrumentation and Measurement, IEEE Transactions on*, 47(5):1180–1186, Oct 1998.
- [7] W. Hauschild and E. Lemke. *High-Voltage Test and Measuring Techniques*. Springer, 2014.
- [8] *IEEE Std 1783, IEEE Guide for Test Methods and Procedures to Evaluate the Electrical Performance of Insulators in Freezing Conditions*, IEEE Standard, 2009.
- [9] M. Farzaneh and W.A. Chisholm. Insulator icing test methods, selection criteria and mitigation alternatives. *Dielectrics and Electrical Insulation, IEEE Transactions on*, 14(6):1462–1473, December 2007.
- [10] A.J. Schwab. *High-voltage measurement techniques*. Monographs in modern electrical technology. M.I.T. Press, 1972.

- [11] Yi Li and M.K. Ediriweera. Measurement uncertainties of impulse parameters due to nonideal step responses of high-voltage dividers. *Instrumentation and Measurement, IEEE Transactions on*, 60(7):2217–2222, July 2011.
- [12] Hong Tang and A. Bergman. Uncertainty calculation for an impulse voltage divider characterised by step response. In *High Voltage Engineering, 1999. Eleventh International Symposium on (Conf. Publ. No. 467)*, volume 1, pages 62–65 vol.1, 1999.
- [13] Ronald H. McKnight, J.E. Lagnese, and Y.X. Zhang. Characterizing transient measurements by use of the step response and the convolution integral. *Instrumentation and Measurement, IEEE Transactions on*, 39(2):346–352, Apr 1990.
- [14] Yi Liu, Fuchang Lin, Guan Hu, and Miao Zhang. Design and performance of a resistive-divider system for measuring fast hv impulse. *Instrumentation and Measurement, IEEE Transactions on*, 60(3):996–1002, March 2011.
- [15] B Racz and A Patocs. Fast high-voltage resistive pulse divider. *Measurement Science and Technology*, 3(9):926, 1992.
- [16] B. Phoaphan, S. Potivejkul, P. Chaisiri, and P. Yutthagowith. Design and construction of a prototype saline solution resistive voltage divider. In *Electrical Engineering/Electronics, Computer, Telecommunications and Information Technology (ECTI-CON), 2013 10th International Conference on*, pages 1–4, May 2013.
- [17] J. Cmiral. *High voltage solution resistive divider for fast transients measurement*. Master thesis, CTU-FEE in Prague (in Czech), 2015.
- [18] E.-P. Suomalainen and J.K. Hallstrom. Onsite calibration of a current transformer using a rogowski coil. *Instrumentation and Measurement, IEEE Transactions on*, 58(4):1054–1058, April 2009.
- [19] B. Djokic. Calibration of rogowski coils at power frequencies using digital sampling. *Instrumentation and Measurement, IEEE Transactions on*, 58(4):751–755, April 2009.
- [20] L. Lu, J. Huang, and Y. Li. A device for calibrating rogowski coils in time domain. *Rev. Sci. Instrum.*, 79(8):085106–1–085106–4, 2008.

- [21] K. Draxler, R. Styblikova, J. Hlavacek, and R. Prochazka. Calibration of rogowski coils with an integrator at high currents. *Instrumentation and Measurement, IEEE Transactions on*, 60(7):2434–2438, July 2011.
- [22] R. Prochazka, J. Hlavacek, Kvasnicka V., and Draxler K. Rogowski coil parameters verification in wide frequency range. In *Proceedings of the 16th International Symposium on High Voltage Engineering*, Cape Town, South Africa, August 2009.
- [23] J. Hlavacek, R. Prochazka, K. Draxler, and V. Kvasnicka. The rogowski coil design software. In *16th IMEKO TC4 Symposium, Exploring New Frontiers of Instrumentation and Methods for Electrical and Electronic Measurements*, Florence, Italy, 2008.
- [24] R. Prochazka, J. Hlavacek, and K. Draxler. Magnetic circuit of a high-voltage transformer up to 10 khz. *Magnetics, IEEE Transactions on*, 51(1):1–4, Jan 2015.
- [25] K. Draxler and R. Styblikova. Using instrument transformers in a wider frequency range. In *Instrumentation and Measurement Technology Conference (I2MTC), 2011 IEEE*, pages 1–4, May 2011.
- [26] R. Prochazka, J. Hlavacek, and K. Draxler. Impulse current transformer with a nanocrystalline core. *Magnetics, IEEE Transactions on*, 49(1):77–80, Jan 2013.
- [27] Leonard B. Loeb and John M. Meek. The mechanism of spark discharge in air at atmospheric pressure. i. *Journal of Applied Physics*, 11(6):438–447, 1940.
- [28] Leonard B. Loeb and J. M. Meek. The mechanism of spark discharge in air at atmospheric pressure. ii. *Journal of Applied Physics*, 11(7):459–474, 1940.
- [29] Leonard B. Loeb. Some aspects of breakdown streamers. *Phys. Rev.*, 94:227–232, Apr 1954.
- [30] H. Raether. Die entwicklung der elektronenlawine in den funkenkanal. *Zeitschrift für Physik*, 112(7-8):464–489, 1939.
- [31] I Gallimberti. A computer model for streamer propagation. *Journal of Physics D: Applied Physics*, 5(12):2179, 1972.

- [32] G. Baldo, I Gallimberti, H. N. Garcia, B. Hutzler, J. Jouaire, and M. F. Simon. Breakdown phenomena of long gaps under switching impulse conditions influence of distance and voltage level. *Power Apparatus and Systems, IEEE Transactions on*, 94(4):1131–1140, July 1975.
- [33] Les Reanrdieres Group. Double impulse tests of long airgaps. part 2: Leader decay and reactivation. *Physical Science, Measurement and Instrumentation, Management and Education - Reviews, IEE Proceedings A*, 133(7):410–437, October 1986.
- [34] Les Reanrdieres Group. Double impulse tests of long airgaps. part 3: Voltage front perturbation effects. *Physical Science, Measurement and Instrumentation, Management and Education - Reviews, IEE Proceedings A*, 133(7):438–468, October 1986.
- [35] Les Reanrdieres Group. Double impulse tests of long airgaps. part 4: Effects of pre-existing space charge on positive discharge development. *Physical Science, Measurement and Instrumentation, Management and Education - Reviews, IEE Proceedings A*, 133(7):469–483, October 1986.
- [36] Les Reanrdieres Group. Double impulse tests of long airgaps. part 1: Engineering problems and physical processes: the basis of recent tests. *Physical Science, Measurement and Instrumentation, Management and Education - Reviews, IEE Proceedings A*, 133(7):395–409, October 1986.
- [37] N Goelian, P Lalande, A Bondiou-Clergerie, G L Bacchiega, A Gazzani, and I Gallimberti. A simplified model for the simulation of positive-spark development in long air gaps. *Journal of Physics D: Applied Physics*, 30(17):2441, 1997.
- [38] A Bondiou and I Gallimberti. Theoretical modelling of the development of the positive spark in long gaps. *Journal of Physics D: Applied Physics*, 27(6):1252, 1994.
- [39] I. Gallimberti. The mechanism of long spark formation. *J. Phys. Coll.*, C7(40):193–250, 1979.
- [40] I Gallimberti, G Bacchiega, Anne Bondiou-Clergerie, and Philippe Lalande. Fundamental processes in long air gap discharges. 3:1335–1359, 2002.
- [41] F. A M Rizk. A model for switching impulse leader inception and breakdown of long air-gaps. *Power Delivery, IEEE Transactions on*, 4(1):596–606, Jan 1989.

- [42] Farouk A.M. Rizk. Switching impulse strength of air insulation: leader inception criterion. *Power Delivery, IEEE Transactions on*, 4(4):2187–2195, Oct 1989.
- [43] Farouk A.M. Rizk. Critical switching impulse strength of long air gaps: modelling of air density effects. *Power Delivery, IEEE Transactions on*, 7(3):1507–1515, Jul 1992.
- [44] E.M. Bazelyan and Y.P. Raizer. *Spark Discharge*. Taylor & Francis, 1997.
- [45] M.E. Slama, A Beroual, and H. Hadi. Influence of the linear non-uniformity of pollution layer on the insulator flashover under impulse voltage - estimation of the effective pollution thickness. *Dielectrics and Electrical Insulation, IEEE Transactions on*, 18(2):384–392, April 2011.
- [46] S. Ilhan, A Ozdemir, S.H. Jayaram, and E.A Cherney. Simulations of pollution and their effects on the electrical performance of glass suspension insulators. In *Electrical Insulation and Dielectric Phenomena (CEIDP), 2012 Annual Report Conference on*, pages 803–806, Oct 2012.
- [47] E. Garbagnati, G. Marrone, A. Porrino, D. Perin, and A. Pignini. Switching impulse performance of post insulators in polluted conditions. In *Fifth International Symposium on High Voltage Engineering*, 1987.
- [48] M. Farzaneh, S. Brettschneider, K.D. Srivastava, and S. Y. Li. Impulse breakdown performance of the ice surface. In *High Voltage Engineering, 1999. Eleventh International Symposium on (Conf. Publ. No. 467)*, pages 341–344, 1999.
- [49] T. Guerrero, M. Farzaneh, and J. Zhang. Impulse voltage performance of ice-covered post insulators. In *Annual Report Conference on Electrical Insulation and Dielectric Phenomena*, pages 341–344, 2005.
- [50] V. Jaiswal, M. Farzaneh, and D.A Lowther. Impulse flashover performance of semiconducting glazed station insulator under icing conditions based on field calculations by finite-element method. *Generation, Transmission and Distribution, IEE Proceedings-*, 152(6):864–870, Nov 2005.
- [51] *IEEE Std 1783-2009 Guide for Test Methods and Procedures to Evaluate the Electrical Performance of Insulators in Freezing Conditions*, IEEE Standard, 2009.

- [52] Changiz TAVAKOLI-ZANIANI. *Dynamic Modeling of AC Arc Development on Ice Surfaces*. Ph.D. en Ingénierie, UQAC, 2004.
- [53] G. Bizjak, P. Zunko, and D. Povh. Circuit breaker model for digital simulation based on mayr's and cassie's differential arc equations. *Power Delivery, IEEE Transactions on*, 10(3):1310–1315, Jul 1995.
- [54] King-Jet Tseng, Yaoming Wang, and D.M. Vilathgamuwa. An experimentally verified hybrid cassie-mayr electric arc model for power electronics simulations. *Power Electronics, IEEE Transactions on*, 12(3):429–436, May 1997.
- [55] J.L. Guardado, S.G. Maximov, E. Melgoza, J.L. Naredo, and P. Moreno. An improved arc model before current zero based on the combined mayr and cassie arc models. *Power Delivery, IEEE Transactions on*, 20(1):138–142, Jan 2005.
- [56] H. Boheme and F. Obenaus. Pollution flashover tests on insulators in the laboratory and in systems and the model concept of creepage path flashover. *CIGRE*, 407, 1966.
- [57] H.H. Woodson and A.J. McElroy. Insulators with contaminated surfaces, part ii: Modeling of discharge mechanisms. *Power Apparatus and Systems, IEEE Transactions on*, PAS-89(8):1858–1867, Nov 1970.